Naval Research Laboratory

Washington, DC 20375-5320

Numerical Modeling of Fire Suppression Using Water Mist.
1. Gaseous Methane-Air Diffusion Flames

K. Prasad
C. Li
K. Kailasanath

Center for Reactive Flow and Dynamical Systems
Laboratory for Computational Physics and Fluid Dynamics

C. Ndubizu
R. Ananth
P. Tatem

Naval Technology Center for Safety and Survivability
Chemistry Division

January 19, 1998

19980225 085

DTIC QUALITY INSPECTED

REPORT DOCUMENTATION PAGE

1. AGENCY USE ONLY (Leave Blank)	2. REPORT DATE January 19, 1998	3. REPORT TYPE AND DATES COVERED NRL Memorandum Report

4. TITLE AND SUBTITLE Numerical Modeling of Fire Suppression Using Water Mist. 1. Gaseous Methane-Air Diffusion Flames	5. FUNDING NUMBERS PE — 62121N

6. AUTHOR(S)

K. Prasad, C. Li, K. Kailasanath, C. Ndubizu, R. Ananth, and P. Tatem

7. PERFORMING ORGANIZATION NAME(S) AND ADDRESS(ES) Naval Research Laboratory Washington, DC 20375-5320	8. PERFORMING ORGANIZATION REPORT NUMBER NRL/MR/6410--98-8102

9. SPONSORING/MONITORING AGENCY NAME(S) AND ADDRESS(ES) Office of Naval Research 800 N. Quincy Street Arlington, VA 22217-5660	10. SPONSORING/MONITORING AGENCY REPORT NUMBER

11. SUPPLEMENTARY NOTES

12a. DISTRIBUTION/AVAILABILITY STATEMENT Approved for public release; distribution unlimited.	12b. DISTRIBUTION CODE

13. ABSTRACT (Maximum 200 words)

This report is the first in a series dealing with the numerical modeling of fire suppression using water mist. The focus of this report is on the suppression of gas jet diffusion flames using fine water droplets. A two-continuum formulation is used in which the gas phase and the water mist are both described by equations of the eulerian form. The model is used to obtain a detail understanding of the physical processes involved during the interaction of water mist and flames. The relative contribution of various mist suppression mechanisms is studied. The effect of droplet diameter, spray injection density and velocity on water mist entrainment into the flames and flame suppression is quantified. Droplet trajectories are used to identify the regions of the flame where the droplets evaporate and absorb energy. Finally, the model is used to determine the water required for extinction, and this is reported in terms of the ratio of the water supply rate to the fuel flow rate.

14. SUBJECT TERMS Fire suppression Numerical modeling Diffusion flame Water mist	15. NUMBER OF PAGES 53
	16. PRICE CODE

17. SECURITY CLASSIFICATION OF REPORT UNCLASSIFIED	18. SECURITY CLASSIFICATION OF THIS PAGE UNCLASSIFIED	19. SECURITY CLASSIFICATION OF ABSTRACT UNCLASSIFIED	20. LIMITATION OF ABSTRACT UL

CONTENTS

LIST OF FIGURES

Numerical Modeling of Fire Suppression using Water Mist.
1. Gaseous Methane-Air Diffusion Flames

1. INTRODUCTION

Water as a means of fire suppression has been in use from ancient times. The phase-out of halons and search for alternative technologies that preserve all of the benefits of a clean total flooding agent without the adverse environmental impact has sparked renewed interest in water mist technology. The need for low weight impact replacement sprinkler systems on commercial ships has been driven by International Maritime Organization regulations requiring retrofit of fire suppression systems on most commercial marine vessels. This has also given recent impetus to the development of low water demand, high efficiency mist systems to replace sprinkler systems.

Fine water mist relies on relatively small (less than 200 μm) droplet sprays to extinguish fires. The mechanisms of extinguishment include gas phase cooling (thermal effect), oxygen displacement by steam, wetting of fuel surface and attenuation of radiative heat transfer. Although the usefulness of water mist fire suppression systems has been demonstrated in a wide range of applications and by numerous experimental programs (References [1]- [14]), a widely accepted critical concentration of water droplets required to extinguish a fire is yet to be determined. Factors that contribute to the success or failure of a water mist system for a particular application include droplet size, velocity, spray pattern geometry, momentum and mixing characteristics of the spray jet, geometry and other characteristics of the protected area. At this time the effect of these factors on system effectiveness is not well known. There is no current theoretical basis for the selection of spray characteristics and other important water mist system parameters.

1.1 Literature Review

Extinguishment of jet diffusion flames by the introduction of water sprays at the base of the flame has been studied by a number of investigators [1]- [5]. These flames can be extinguished very efficiently by this technique since the normal air entrainment process assures that all the water spray added adjacent to the flame is actually transported into the flame. The water required for extinguishment is reported in terms of the ratio of the water supply rate to the fuel supply rate at extinction. These ratios range from 1.5 to 10. While no systematic evaluation of droplet sizes on the water/fuel ratio at extinction has been performed, the available data indicate that the ratio is reduced with decreasing droplet size for laboratory flames. Large scale flames could be extinguished with a water/fuel ratio of 1.6. However, ratios of up to 10 may be required depending on the orientation and geometry of the spray nozzles. While drop size information was not given, the nozzles used in the experiments were expected to produce droplets on the order of 1000μm diameter. Similar results were obtained for laboratory flames with droplet sizes of

$15 \mu m$. These studies also indicate the reduction in flame temperature which occurs in flames with sub-extinguishing application rates of water.

The available research in water spray fire extinguishment was reviewed by Rashbash [6] and by Tatem et al. [7]. Rashbash et al. [8]- [9] described two basic mechanisms for extinguishment of liquid fuel fires : gas phase flame extinction and surface cooling. Gas phase extinction was observed to be very rapid while surface cooling was much slower due to the need for water to reach the liquid surface and cool the liquid to below its firepoint temperature. Fundamental aspects of solid fuel fire extinction by water have been addressed by several researchers [10]- [12]. These works have focussed on the effect of water application to the fuel surface and the need for development of efficient water based systems for suppressing fires. McCaffrey [3] has reviewed the available data and appropriate literature concerned with the application of water sprays as a jet diffusion flame suppression/extinguishment agent. Small pneumatic atomizing nozzles using H_2 gas, both as the flame source as well as the atomizing driver, have been used to scale high momentum jet flames and to study the effect of water on the flame. The effect of flame temperature reduction due to water sprays has been observed to correlate with a single spray parameter-the median drop diameter. The effect of adding water spray to the gas flow below the base of a lifted flame is to shift or raise the flame above its normal position and to lower peak flame temperature and radiation levels. Extinguishment near blow-off was observed to be due to shift in flame position. Though McCaffrey did not perform such systematic measurements for methane flames, the general trends are expected to be similar to those of hydrogen flames. It was observed that for hydrogen flames that the maximum flame temperature per unit mass of water per unit mass of fuel was reduced from 150 to $50C$ as the water/fuel ratio increased from 0 to 10. The degree of cooling was also a direct function of the drop size with higher cooling effects associated with smaller droplets.

There has been very little theoretical or experimental work to develop an understanding of gas phase extinguishment of fires. The earliest study of the interaction of flames and water mist was performed by Seshadri [15]. He studied counterflow heptane and methanol flames with an oxidizer stream made up of oxygen, nitrogen and water mist. This work was of a preliminary nature in that only a single water mist flow rate and drop size distribution was used. Based on extinction oxygen mass fractions as a function of strain rate, he deduced one step kinetic parameters for these systems. Based on the similarity of the kinetic parameters, he concluded that water had only a thermal effect. No detailed flame measurements or droplet sizes were reported. Lentati and Chelliah [16] have studied the effect of sodium bicarbonate particle size in extinguishing heptane-air flames. The dynamics of highly sooting fires in unbounded domains have been investigated by Mell et al. [17]. McGratten and Stroup [18] have numerically investigated conditions under which vents and draft curtains are beneficial, and under which they are detrimental, to the performance of a sprinkler system in large enclosures. Parametric studies [19] have been performed to predict the actual delivered densities of early suppression fast response sprinklers in heptane spray fire scenarios.

Ewing et al. [21]- [22] have evaluated the role of thermal processes in the effectiveness of a wide range of extinguishing agents. Their work included experimental investigations of dry chemical agents with critical particle sizes ranging from $20 - 50 \mu m$. They observed that particle sizes below the critical size were fully decomposed in the flame while larger particles were less effective since they were not fully decomposed in the flame. The work of Ewing clearly shows that dry chemicals are on a weight bases the most effective fire extinguishing agents available. They found that condensed

phase agents with large heats of gasification (evaporation or decomposition) would be expected to be very effective agents. They proposed that heat extraction from the combustion region of the flame sheet is critical to flame extinction. They divide the flame into a preheat region and a combustion region and have shown that flame extinction is governed by heat extracted from the combustion region. Since dry chemical agents and water droplets can actually penetrate the preheat region and are largely decomposed or evaporated in the combustion region, these agents are more effective. While these results provide interesting and potentially fruitful directions for research and development, there is a definite need for additional detailed experimental and computational work to develop an understanding of the interactions of water mist droplets with a flame and the detailed processes involved in extinction.

Numerical studies with water mist in a premixed stagnation point methane-air flame have been reported by Chen and Rogg [23]. Chen et al. [24] also presented numerical results for a counterflow methane/air diffusion flame with heptane droplets added to the fuel stream. As expected the volume fraction of water mist at extinction is a function of the strain rate. The temperature in the flame was a direct function of the mist concentration and the droplet evaporation time was predicted. Atreya [25] has observed similar results for methane counterflow diffusion flames. In addition, he found that the burning rate is enhanced at low water addition rates and is ultimately decreased and the flame extinguished at higher application rates.

The overall objective of this study is to develop and apply a numerical model for studying the underlying processes involved in suppression of fires with water mist. This report presents numerical results on the interaction of water mist with diffusion flames along with experimental validation of the numerical model. The model is then used to understand the relative contribution of the various mechanisms of extinction of flames subjected to a fine water mist. The model provides a detailed understanding of droplet dynamics in a 2-D flow field for the study of flame suppression, extinguishment and mist entrainment into a diffusion flame. The degree of mist entrainment into the flame and its dependence on droplet diameter and spray injection velocity is determined. Numerical simulations have been performed to evaluate the decrease in flame temperature as a function of droplet number density. Droplet trajectories are used to identify the regions of the flame (preheat zone, combustion zone or plume zone) where the droplets evaporate and absorb energy. The droplet diameter and the velocity of the droplet required to penetrate the flame under a local application scenario are also determined. Most importantly the model is used to determine the amount of water required for extinguishment, reported in terms of the ratio of the water supply rate to the fuel supply rate at extinction, as a function of droplet diameter. Both local application scenarios and a quasi total flooding scenario have been considered.

The next section describes the governing equations that have been used to study the flow above a 2-Dimensional Wolfhard Parker burner and the interaction of water mist with the diffusion flame. We have considered a two-continuum formulation, wherein the gas properties and the droplet properties are described by equations in the Eulerian form. The next section also describes the single step reaction model that have been used to simulate the chemical reactions between the fuel and oxidizer species and a sectional approach that has been used to predict the movement of the fine water droplets along with The numerical schemes used for time marching solutions of the governing equations (gas phase and the liquid phase) along with the initial and boundary conditions used, have been briefly discussed. The section dealing with "Results and Discussion" describes the various simulations and parametric variations that were performed for studying the

effect of water mist on diffusion flames. The focus of this section is on the effect of droplet size on suppression of diffusion flames and the relative contribution of the various suppression mechanisms. The experimental setup is discussed and validation of the numerical model with the experimental results has also been provided. The degree of mist entrainment into the flame and its dependence on droplet diameter and spray injection velocity is determined. We conclude by describing the key accomplishments of this work along with the directions of our future work on this subject.

2. MATHEMATICAL AND NUMERICAL MODEL

2.1 Objective of the Model

Detailed modeling of gas-phase reactive flows is based on a generally accepted set of time-dependent coupled partial differential equations maintaining conservation of total mass, momentum, total energy and individual species density. These equations describe the convective motion of the fluid, the chemical reactions among the constituent species, and the diffusive transport processes such as thermal conduction and molecular diffusion.

2.2 Gas Phase Equations

A strong conservation form of the two-dimensional, unsteady, compressible Navier-Stokes equations, used to describe gas phase reactive flow systems can be written as follows [27], [28], [29].

$$\frac{\partial \rho}{\partial t} + \frac{\partial \rho u}{\partial x} + \frac{\partial \rho v}{\partial y} = \dot{m}_{evap}, \tag{1}$$

$$\frac{\partial (\rho u)}{\partial t} + \frac{\partial (\rho u^2 + P)}{\partial x} + \frac{\partial (\rho u v)}{\partial y} = \frac{\partial \tau_{xx}}{\partial x} + \frac{\partial \tau_{xy}}{\partial y} + \dot{S}_x, \tag{2}$$

$$\frac{\partial (\rho v)}{\partial t} + \frac{\partial (\rho u v)}{\partial x} + \frac{\partial (\rho v^2 + P)}{\partial y} = \frac{\partial \tau_{yx}}{\partial x} + \frac{\partial \tau_{yy}}{\partial y} - \rho g + \dot{S}_y, \tag{3}$$

$$\frac{\partial (\rho E)}{\partial t} + \frac{\partial ((\rho E + P)u)}{\partial x} + \frac{\partial ((\rho E + P)v)}{\partial y} = \frac{\partial (\tau_{xx} u)}{\partial x} + \frac{\partial (\tau_{xy} u)}{\partial y} + \frac{\partial (\tau_{yx} v)}{\partial x} + \frac{\partial (\tau_{yy} v)}{\partial y}$$
$$+ \frac{\partial q_x}{\partial x} + \frac{\partial q_y}{\partial y} - \rho g v + Q_{chem} + Q_{rad} + Q_{evap}, \tag{4}$$

$$\frac{\partial \rho_k}{\partial t} + \frac{\partial (\rho_k u)}{\partial x} + \frac{\partial (\rho_k v)}{\partial y} = -\frac{\partial (\rho_k U_k)}{\partial x} - \frac{\partial (\rho_k V_k)}{\partial y} + \dot{m}_{k,evap} + \dot{\omega}_k, \quad k = 1, 2, \dots, N. \tag{5}$$

In these equations x and y denote the independent spatial coordinate and t denotes the temporal coordinate; ρ the mass density; ρ_k the density of the k_{th} species; u and v are the x and y components of the fluid bulk velocity; P, the pressure; E, the total energy of the fluid per unit mass; g, the gravitational body force per unit mass; U_k and V_k are the x and y components of the diffusion velocity for the k_{th} species; τ_{xx}, τ_{xy}, τ_{yy} are the components of the stress tensor for newtonian fluid in rectangular coordinate; q_x and q_y are the x and y components of the heat-flux vector. $\dot{m}_{evap}$ is the source term arising in the mass conservation equation due to evaporation of the water droplets, resulting in the production of water vapor. The corresponding term in the H_2O gas phase species

conservation equation is represented by $\dot{m}_{k,evap}$. $\dot{\omega}_k$ is the rate of production of the kth species due to chemical reactions. Similarly Q_{chem} is an exothermic source term in the energy equation arising due to the oxidation of fuel molecules, whereas Q_{evap} represent absorption of energy due to drop evaporation; Q_{rad} is the radiative heat loss term. $\dot{S}_x$ and $\dot{S}_y$ are the source terms arising in the x and y momentum equations representing the cumulative drag force exerted by the various droplet sections on the gas phase.

The viscous stress terms are related to the rate of strain through the stress-strain relationship,

$$
\begin{aligned}
\tau_{xx} &= \mu \left[\frac{4}{3} \frac{\partial u}{\partial x} - \frac{2}{3} \frac{\partial v}{\partial y} \right], \\
\tau_{xy} &= \mu \left[\frac{\partial u}{\partial y} + \frac{\partial v}{\partial x} \right], \\
\tau_{yy} &= \mu \left[\frac{4}{3} \frac{\partial v}{\partial y} - \frac{2}{3} \frac{\partial u}{\partial x} \right],
\end{aligned}
\tag{6}
$$

where μ is the dynamic viscosity. The components of the heat flux vector contain contribution due to the heat conduction and the interdiffusion process, and can be expressed as

$$
\begin{aligned}
q_x &= -\lambda \frac{\partial T}{\partial x} + \sum_{k=1}^{N} (h_k \rho_k U_k), \\
q_y &= -\lambda \frac{\partial T}{\partial y} + \sum_{k=1}^{N} (h_k \rho_k V_k),
\end{aligned}
\tag{7}
$$

where λ is the thermal conductivity of the fluid mixture and h_k is the enthalpy per unit mass for the k_{th} species.

The total energy per unit mass E is defined as the sum of internal energy e and the kinetic energy as follows

$$
E = e + \frac{1}{2}(u^2 + v^2),
\tag{8}
$$

The internal energy is related to the thermodynamic pressure P through the ideal gas equation of state

$$
P = R_o T \sum_{k=1}^{N} \frac{\rho_k}{W_k},
\tag{9}
$$

and the caloric equation of state

$$
e = \sum_{k=1}^{N} Y_k h_k - \frac{P}{\rho},
\tag{10}
$$

$$
h_k = \int_{T^o}^{T} C_{p,k} dT,
\tag{11}
$$

In these equations R_o is universal gas constant; W_k, the molecular weight of the kth species and $\Delta h_{f,k}^0$ are the heats of formation for the various species at the reference temperature T^o.

2.3 Thermodynamics

The diffusion velocities U_k and V_k for the kth species are computed using Fick's Law, without solving the complete matrix problem associated with a multi-component system.

$$U_k = -\frac{1}{X_k}\mathcal{D}_{km}\frac{\partial X_k}{\partial x} \quad k = 1, 2, \ldots, N,$$

$$V_k = -\frac{1}{X_k}\mathcal{D}_{km}\frac{\partial X_k}{\partial y} \quad k = 1, 2, \ldots, N. \tag{12}$$

Here, $\mathcal{D}_{km}$ is the diffusion coefficient for species k diffusing into the mixture and X_k is the mole fraction of the kth species. The resulting diffusion velocities are corrected to satisfy the requirement that the diffusion velocities do not introduce any net bulk velocity to the fluid. The diffusion velocities are computed subject to the constraint equations

$$\sum_{k=1}^{N} \rho_k U_k = 0,$$

$$\sum_{k=1}^{N} \rho_k V_k = 0, \tag{13}$$

The mole fractions can be related to the mass fraction Y_k through the auxiliary relation

$$X_k = \frac{Y_k/Wk}{\sum_{k=1}^{N} Y_k/W_k}, \quad k = 1, 2, \ldots, N. \tag{14}$$

The mixture diffusion coefficient $\mathcal{D}_{km}$ of the kth species is related to the binary diffusion coefficient $\mathcal{D}_{kl}$ of species k diffusing into species l. The binary diffusion coefficients are calculated from kinetic theory and are in the following form

$$\mathcal{D}_{kl} = A_{kl}T^{B_{kl}}/n, \quad k,l = 1, 2, \ldots, N, \tag{15}$$

where A_{kl} and B_{kl} depend on species k and l. Values for A_{kl} and B_{kl} have been tabulated by Kailasanath et al. [30]. The diffusion coefficient of species k in a mixture of N species is calculated according to

$$\mathcal{D}_{km} = \frac{1 - Y_k}{\sum_{l=1, l\neq k}^{N} \frac{X_l}{\mathcal{D}_{k,l}}}, k = 1, 2, \ldots, N. \tag{16}$$

The mixture thermal conductivity λ is obtained by combining the thermal conductivities of the individual gases λ_k that are present in the mixture. The species thermal conductivity, λ_k, are estimated theoretically from kinetic theory over the temperature range $300K$ to $3300K$, and these values were fit to a third-order polynomial. The mixture thermal conductivity is then calculated using the expression from Kee et al. [31]

$$\lambda = \frac{1}{2}\left[\sum_{k=1}^{N} X_k\lambda_k + \frac{1}{\sum_{k=1}^{N} \frac{X_k}{\lambda_k}}\cdot\right] \tag{17}$$

The dynamic viscosity of a single species μ_k can be obtained from kinetic theory and is fitted over a suitable temperature range using a third order polynomial. The mixture dynamic viscosity is calculated using the expression by Wilke [32],

$$\mu = \sum_{k=1}^{N} \frac{X_k \mu_k}{\sum_{j=1}^{N} X_j \phi_{kj}}, \tag{18}$$

where,

$$\phi_{kj} = \frac{1}{\sqrt{8}} \left(1 + \frac{W_k}{W_j}\right)^{-\frac{1}{2}} \left(1 + (\frac{\mu_k}{\mu_j})^{\frac{1}{2}} (\frac{W_j}{W_k})^{\frac{1}{4}}\right)^2. \tag{19}$$

2.4 Kinetics

Ideally, we would like to simulate the chemical reactions by including a detailed set of elementary reactions to describe the production of the individual species and the energy release in the flame. However, the cost of computer time and memory required to track the individual species makes this prohibitive for problems in which parametric studies are planned. Instead, the chemical reaction and energy-release process for methane-air combustion is described phenomenologically based on a single step reaction,

$$CH_4 + 2O_2 \rightarrow CO_2 + 2H_2O, \tag{20}$$

using a finite-rate, quasi-global Arrhenius expression. Westbrook et al. [33] has developed simplified reaction mechanisms for the oxidation of hydrocarbons using a laminar flame model and has prescribed an overall rate of consumption of methane as

$$\frac{d[CH_4]}{dt} = -1.3E8exp(-48400/RT)[CH_4]^{-0.3}[O_2]^{1.3}. \tag{21}$$

The above expression is used to compute the depletion of methane. The stoichiometric coefficients provided in Equation (20) is then used to compute the corresponding changes in the concentration of oxygen, carbon dioxide, water vapor and nitrogen. The heat release term Q_{chem} appearing in the energy equation 4 is determined from

$$Q_{chem} = -\Delta H_c \frac{d[CH_4]}{dt}, \tag{22}$$

where ΔH_c is the heat of combustion for the single step global chemical reaction per unit mass of fuel. The heat of combustion is computed using the stoichiometric coefficients and the heat of formation of the various species as follows,

$$\Delta H_c = \sum_{k=1}^{N} (\nu_k'' - \nu_k') \Delta h_{f,k}^0, \tag{23}$$

where, ν_k' and ν_k'' are the stoichiometric coefficients of the kth species as a reactant and product respectively and $\Delta H_{f,k}^0$ is the heat of formation of the kth species.

2.5 Water mist model

In this section we describe the approach that we have used in formulating the system of differential equations that govern the spray and gas behavior in a coupled manner. We will consider a two-continuum formulation, wherein the gas properties and the droplet properties are each described by equations in the Eulerian form. This Eulerian-Eulerian form is useful when resolution is desired only on a scale larger than the average distance between the droplets. In this approach the droplet properties are treated as if they were continuous in the domain as the gaseous properties [34], [35]. The droplet property at a point in space and time represents the average value over many droplets in the neighborhood of that point.

The size distribution of the spray droplets can be described by the concentration of discrete droplets of various sizes per unit volume of fluid $n_i(x, y, t)$ as a function of spatial coordinates x, y and of time t where $i = 1, 2, \ldots$. The magnitude of the integer i represents the total number of discrete droplet sizes. The vaporization process [36], [37] can be described by a set of coupled differential equations for the concentration of the discrete droplet sizes

$$\frac{\partial n_i}{\partial t} + u_{l,i}\frac{\partial n_i}{\partial x} + v_{l,i}\frac{\partial n_i}{\partial y} = -E_i n_i + E_{i+1} n_{i+1}, \quad i = 1, 2, \ldots, \tag{24}$$

where $u_{l,i}$ and $v_{l,i}$ are the x and y components of the velocity vector of the ith droplet size and E_i is the frequency of the molecule evaporation. This frequency highly depends on the surface area of the droplet and on the temperature of the ambient gas in addition to other flow parameters. Since the total number of droplet sizes needed to simulate actual fuel sprays can be immense, sectional conservation equations have been developed. This method is based on dividing the droplet size domain into sections and dealing only with one integral quantity in each section. This sectional representation has the advantage that the integral quantity is conserved within the computational domain and the number of conservation equations is substantially reduced so as to equal the number of sections.

We divide the entire droplet size domain into M arbitrary sections, and define Q_j to be an integral quantity of the spray with the jth section. Thus

$$Q_j = \int_{v_{j-1}}^{v_j} vn\,dv, \quad j = 1, 2, \ldots, M, \tag{25}$$

where $n(v, t)$ is the number concentration function and v_{j-1} and v_j denote the volumes of the smallest and largest droplets, respectively, in section j. Using equation 25 in equation 24 the sectional conservation equation can be rewritten as

$$\frac{\partial Q_j}{\partial t} + u_{l,j}\frac{\partial Q_j}{\partial x} + v_{l,j}\frac{\partial Q_j}{\partial y} = -C_j Q_j + B_{j,j+1} Q_{j+1}, \quad j = 1, 2, \ldots, M, \tag{26}$$

where the sectional coefficients $B_{j,j+1}$ and C_j are described in the following forms:

$$B_{j,j+1} = \left(\frac{v_{k_j}}{v_{k_j+1}}\right)\frac{E(v_j, T)}{v_{j+1} - v_j}, \tag{27}$$

$$C_j = \left(\frac{v_{k_{j-1}}}{v_{k_{j-1}+1}}\right)\frac{E(v_{j-1}, T)}{v_j - v_{j-1}} + \frac{1}{v_j - v_{j-1}}\int_{v_{j-1}}^{v_j}\frac{1}{v}E(v, T)\,dv, \tag{28}$$

where $E(v, T)$ is the volume rate of vaporization of a droplet of volume v.

The mass or volume rate of vaporization of each single droplet is proportional to the droplet diameter d (the d^2 law). Thus

$$E(v, T) = (\pi/4)E(T)d, \tag{29}$$

where $E(T)$ is the vaporization or burning rate coefficient, which depends on the temperature of the surrounding gas, the diffusivity and other properties of the droplet and its surroundings. For the present calculations, the burning rate coefficient value of $7.6E3\mu m^2/s$ was assumed for fine water mist particles [38], [27]. Assuming a d^2 law to re-express the sectional vaporization coefficients in terms of droplet diameters and assuming a continuous division into sections the coefficients can be rewritten as

$$B_{j,j+1} = \frac{3}{2}E(T)\left[\frac{d_{L,j+1}}{d_{U,j+1}^3 - d_{L,j+1}^3}\right], \quad j = 1, 2, \ldots, M-1,$$

$$C_j = \frac{3}{2}E(T)\left[\frac{d_{L,j}}{d_{U,j}^3 - d_{L,j}^3} - \frac{3(d_{U,j} - d_{L,j})}{d_{U,j}^3 - d_{L,j}^3}\right], \quad j = 1, 2, \ldots, M. \tag{30}$$

Each of the droplet sections is assumed to have its own unique velocity different from that of the gas phase. Momentum conservation equations are formulated for each droplet section and are coupled to those of the gas phase through the phase interaction terms (drag terms). The droplet drag equations are given by

$$\frac{\partial u_{l,j}}{\partial t} + u_{l,j}\frac{\partial u_{l,j}}{\partial x} + v_{l,j}\frac{\partial u_{l,j}}{\partial y} = F_{x,j}, \quad j = 1, 2, \ldots, M,$$

$$\frac{\partial v_{l,j}}{\partial t} + u_{l,j}\frac{\partial v_{l,j}}{\partial x} + v_{l,j}\frac{\partial v_{l,j}}{\partial y} = F_{y,j} - g, \quad j = 1, 2, \ldots, M, \tag{31}$$

where $F_{x,j}$ and $F_{y,j}$ are the x and y components of the drag force acting on the jth sectional velocity modeled based on Stokes Law. The gas phase momentum source terms $\dot{S}_x$ and $\dot{S}_y$ are equal and opposite to the sectional density weighted sum of $F_{x,j}$ and $F_{y,j}$ respectively.

2.6 Numerical Algorithm

The governing equations are rewritten in terms of finite-volume approximations on an Eulerian mesh and solved numerically for specific boundary and initial conditions. A complete solution to these governing equations require solving the terms for each of the individual processes, as well as accounting for the interaction among the processes. The solution approach consists of separate algorithms for each of the individual processes, which are then coupled together by the method of time-step splitting. The algorithms for convection, thermal conduction, molecular diffusion, viscosity and the coupling of the individual processes have been previously discussed in detail [39], [40].

The fluid convection is solved with a high-order implicit algorithm, Barely Implicit Correction to the Flux-Corrected Transport (BIC-FCT) [39], that was developed to solve the convection equations for low-velocity flows. The Flux-Corrected Transport (FCT) [41] algorithm itself is an explicit,

finite-difference algorithm that is constructed to have fourth-order phase accuracy. Through a two-step predictor-corrector algorithm, FCT ensures that all conserved quantities remain monotone and positive. The FCT procedure is to first modify the properties of a high-order algorithm by adding diffusion during a convection step and then to subtract out the diffusion in an antidiffusion phase. In addition, fluxes are limited to ensure that no new unphysical maxima or minima are added during the convection process. However, because FCT is an explicit algorithm, the numerical time-step required for accuracy and stability is limited by the velocity of sound according to the CFL condition. To filter out the sound waves from the convection equations and therefore remove the sound-speed (Courant) limitation on the time-step, the convection equations are usually solved implicitly. The BIC-FCT algorithm was developed so that the time step is limited by the fluid velocity and not the sound speed. This implementation is particularly useful for slowly evolving flows because one BIC-FCT time-step requires the same amount of computer time as one regular FCT explicit time step, but the size of the timestep might be a factor of 50-100 times greater. The reaction rate equations involving the arrhenius terms are solved using an implicit trapezoidal scheme with time step splitting over the largest fluid dynamic time step.

A specific solution of the reactive flow equations is determined by the initial conditions and the boundary conditions that describe the geometry of the system and exchange of mass, momentum and energy occurring between the system and the rest of the physical world. The total density, u and v momentum and the various species densities are prescribed at the inflow boundary. At the outflow boundary, the normal gradients of total density, species densities and momentum was assumed to be zero. The pressure at large distances from the burner surface is assumed to be equal to the ambient pressure. A symmetric boundary condition was employed at the center line of the computational domain by use of anti-symmetric reflection of tangential velocity v, and symmetric reflection of all other variables. A slip wall boundary condition is employed at the lateral boundary by assuming that the flux of all transported properties across the wall is zero. For a diffusion flame computation, the initial conditions at each point in the domain were the same as inlet conditions. The spray injection densities and the two components of the velocity vector are specified at the inflow boundary. Again symmetric boundary conditions are employed for the liquid phase at the center line and slip wall conditions are employed at the edge of the burner.

The computational domain consists of a stretched 96×128 grid, concentrated near the contact point of the fuel and the oxidizer. The smallest grid cell is a $0.5mm \times 0.5mm$ square cell. Numerical simulations were performed by halving the grid size to check for accuracy and consistency of the algorithms. The algorithms have been optimized for efficient performance on vector machines. Typical computational time on a C-90 single processor machine was approximately 4 hours to reach a steady state solution.

3. RESULTS AND DISCUSSION

The governing equations described earlier were solved using the numerical models briefly discussed above, to study methane-air diffusion flames stabilized above a Wolfhard Parker burner. Fine water mist is introduced along with the co-flowing air to study the interaction and subsequent suppression of these flame with water mist. The numerical results have been compared with experimental data obtained using a similar geometry.

3.1 Comparison to Experimental Data

The key component of the experimental setup is a modified Wolfhard-Parker burner which is shown schematically in Figure 1. The burner slot is 75 *mm* long, 10 *mm* wide and 150 *mm* deep. It has two identical oxidizer channels 82 *mm* long, 35 *mm* wide and 150 *mm* deep on each side. Beside each oxidizer channel is the mist generation chamber where mist is produced with commercial low flow Delavan nozzles. A fraction of the mist generated in this chamber is entrained into the air stream. The slot opening is adjustable to control the quantity of mist entrained into the air stream. Mist flow rate is determined by covering the channel for a given time with a very fine screen. The mass of mist collected during this period gives a measure of the mist flow rate out of the air channel. To introduce steam along with the air co-flow, an electrically heated fine screen is used to collect and evaporate the mist droplets before they exit from the air channel. The fuel slot is filled with fine clean sand to produce a near plug flow condition. Similarly, three layers of fine screen are used to produce a uniform air velocity profile in each air channel. In the current experiments, the average exit velocity of the fuel is 2.81*cm/sec* and the average exit velocity of the air is 18.1*cm/sec*. A quartz glass shield, 47 cm long and 27 cm high sits on the burner on either side to protect the flame from any external disturbances. The flame temperature is measured with a 50 μm diameter fine platinum/platinum - 13% - rhodium thermocouple which is computer controlled by a Newport 3D positioning instrument The droplet diameter is characterized using the Malvern particle analyser. Infrared images of the flame are also obtained using the Agema Thermovision 870 scanner, calibrated with a blackbody source and with the thermocouple temperature measurements.

Figure 2 shows comparison of numerically computed and experimentally measured temperature profiles for the the base case methane - air diffusion flames. The comparison has been made at a height of 5, 15, 30 and 55 mm above the burner surface. At each height the numerically computed temperature profile compares favorably with the thermocouple temperature measurements [43]. The numerically computed values are very sensitive to the boundary conditions that are imposed at the burner surface. The small differences in temperature profiles between the numerical and experimental results are due to the idealization of the boundary conditions observed in the experiments. It is not possible to mathematically characterize the precise boundary conditions present in the experiments. Therefore, experimentally determined values were used as boundary conditions in the numerical solution procedure. Once set, the same boundary conditions have been used for all the cases discussed in this paper.

Next, the effect of nitrogen dilution on methane - air diffusion flame was studied. Nitrogen was introduced along with the air co-flow resulting in different levels of nitrogen. Figure 3 shows comparison of numerical and experimental results for CH_4 and 18.2%O_2, 81.8%N_2 mole fraction diffusion flame. Numerically computed temperature profiles are compared with experimental results at a height of 6, 40, 46 and 50 mm above the burner surface. Again the agreement between the computed and experimentally measured values is very good. Additional cases with different amounts of nitrogen dilution (Figure 4 for the case of 16.0%O_2, 83.5%N_2 mole fraction) have also been simulated and have been compared with experimental results. As nitrogen dilution increases the diffusion flame appears to become broader and taller due to a shift in the location of the stoichiometric surface towards the oxidizer jet. As expected, the maximum flame temperature reduces with increasing levels of nitrogen dilution until a critical dilution level at which the flame extinguishes. This effect is similar to the "oxygen displacement effect" observed during the interaction of water mist with diffusion flame (discussed later in the text). The exact level of nitrogen dilution

for extinction can be predicted more accurately by using detailed finite rate kinetics for modeling the oxidation of the fuel molecule. Due to the very high computational costs associated with using finite rate kinetics, it is not possible to perform the large number of parametric studies required for optimizing the water mist spray characteristics. The use of single step chemistry is shown to reproduce the correct trends as observed in the experiments, while keeping the computational costs low.

3.2 Base Case Diffusion Flame Results

One of the advantages of numerical simulations is that a detailed spatial characterization of the flame and flow field can be obtained with little additional cost or effort. In addition, quantities such as heat release rate can be predicted which are difficult to obtain through experiments. Such detailed numerical diagnostics will be used to understand the interaction between water mist and the flame. Figure 5 shows contour plots of temperature (K) and heat release rate ($Joules/mtr^3/sec$) above a two-dimensional methane-air diffusion flame burner. These numerical simulations were performed for the burner geometry and flow conditions described earlier. The temperature contours indicate the presence of a very thin flame sheet which closes above the fuel duct. The height of the flame is roughly $7cm$. The maximum flame temperature is $1970K$, which agrees well with experimental results [43], [44]. The heat release rate profile indicates the region of rapid exothermic chemical activity. This profile identifies the location of the flame sheet where the fuel and the oxidizer species come together in stoichiometric proportions, react exothermically and produce product species. Figure 6 shows contour plots of methane (CH_4) and oxygen (O_2) density (kg/mtr^3) above the burner surface. Due to the fuel lean conditions in which these simulations were performed, methane is completely consumed. The unused oxygen flows out of the computational domain along with other product species and diluent gases. Figure 7 shows density profiles of the product species, carbon-dioxide (CO_2) and water vapor (H_2O). Figure 8 shows the velocity vectors and streamline pattern. The velocity vectors have been color coded with red showing the highest gas speed and blue showing the lowest gas velocity. The direction of the arrows shows the direction of the velocity vector. The streamline pattern clearly indicates the entrainment of oxidizer along with the suppressants into the diffusion flame. Both the streamlines and the velocity vectors bend into the flame due to the entrainment of air into the diffusion flame. When similar calculations were performed with the buoyancy terms set to zero, no such entrainment or bending of the streamlines into the flame was observed. Infact, the streamlines under zero gravity conditions tend to diverge away from the flame due to expansion of the hot gases.

3.3 Interaction of Water Mist with Flame

The primary goal of the present research is to study the interaction of water mist with diffusion flames. With the confidence gained by the comparison with experimental data, a series of numerical simulations were performed to determine the underlying processes involved in suppression of flames with water mist. Water mist was introduced along with the air co-flow. The spray velocity at the burner exit was set at $25cm/sec$. Figure 9 shows temperature and heat release rate profiles for 50μ droplets injected uniformly over the length of the air channel. The spray injection density was held fixed at $2000drops/cm^3$. The maximum flame temperature reduces from $1970K$ in the base case to $1795K$ when subjected to 50μ water droplets. The predicted flame height increases from $7cm$ for the base case to $9cm$ when subjected to fine water mist. The temperature and heat release rate profiles indicate an increase in flame height and flame suppression due to the sub-extinguishing application

rates of water mist. The heat release rate profile also indicates the presence of an endothermic heat release rate profile (negative value) showing the approximate location of evaporation of the droplets. When the droplets are introduced parallel to the air co-flow, the evaporation time at the flame sheet was much smaller than the rate of entrainment. For the conditions that have been tested, we did not observe any droplets that could survive the very high temperatures at the flame and penetrate through the diffusion flame. Figure 10 shows similar contours of temperature and heat release under the application of 150μ water droplets and a spray injection density of $100 drops/cm^3$. Flames subjected to water mist are taller and broader than the base case methane-air diffusion flames. The flame height increases by approximately $2cm$ for this case. The maximum flame temperature reduces from $1970K$ in the base case to $1905K$ when subjected to 150μ water droplets. The endothermic values (-ve numbers) in the heat release rate contours are approximately two orders of magnitude smaller than the exothermic values. However the area occupied by the endothermic contours is much larger than that of the exothermic regions. Although the evaporation time is proportional to the square of the droplet diameter, the characteristic time for decrease of the relative velocity due to the drag forces is also proportional to the square of the droplet diameter. As a result with increasing droplet diameter we do not expect the droplets to penetrate the high temperatures of the flame sheet as long as they are introduced in a co-flow manner.

Numerical simulations have been performed to ascertain the effect of changing the injection spray density on methane-air diffusion flames. Figure 11 shows temperature contours for various spray injection densities of 1000, 2000, 3000 and 4000 $drops/cm^3$ of 50μ water mist droplets. As in the previous simulations the spray is injected along with the air co-flow perpendicular to the burner surface. As the spray injection density increases more and more water droplets entrain into the diffusion flame and this results in larger suppression as shown by the reduction in flame temperature. We also observe that as the spray injection density increases, the flame becomes taller and broader (fatter), resulting in larger flame surface area. This result is similar to the one observed under nitrogen and steam dilution of the diffusion flame. The flame height increases from $7cm$ for the base cases flame to about $9cm$ for the $2000 drops/cm^3$ case and to $11cm$ for the injection of $4000 drops/cm^3$ into the co-flow. The initial injection velocity of the droplets was held fixed at $25cm/sec$ for all spray densities. The droplets are divided into five sections (as discussed in section dealing with mathematical formulation) as follows : $0-10\mu$, $10-20\mu$, $20-30\mu$, $30-40\mu$ and $40-50\mu$. Droplet section densities for three of the five sections have been shown in Figure 12. These contours show the location of maximum density and position where these droplets evaporate to form smaller and smaller droplets (sections). The injected spray is a monodisperse spray and consists entirely of 50μ droplets. These droplets convect along with the air co-flow. Some of these droplets evaporate and form smaller droplet sections while others appear to convect out of the computational domain. The droplets that entrain into the diffusion flame evaporate and form smaller sections, resulting in a very large density of the smaller sections very close to the diffusion flame. As a result, the profiles show a very distinct cascading effect in which larger diameter droplets show maximum concentration further away from the diffusion flames, whereas smaller diameter droplets show maximum concentration closer to the diffusion flame.

Figure 13 shows similar droplet section density contours for the injection of 150μ droplets. In this case the droplets are again divided into five sections of $0-30\mu$, $30-60\mu$, $60-90\mu$, $90-120\mu$ and $120-150\mu$. Again the injected spray is a monodisperse spray consisting entirely of 150μ droplets. Unlike the earlier case of 50μ droplets, in this case the $120-150\mu$ section advects with the gas phase only for a very small distance above the burner surface. Beyond this point

the section density and section velocity are zero. This is because the drag force acting on these droplets is not able to counter balance the weight of these droplets and as a result the droplet velocity continuously reduces. When the droplets are injected at higher initial inlet velocity, it was observed that the droplets were able to reach a higher distance above the burner surface due to the larger initial momentum. The smaller sections again show profiles similar to those observed with the 50μ droplet case.

3.4 Droplet Dynamics

The numerical model was used to obtain a detailed understanding of the droplet dynamics in a 2-dimensional flow field and interaction / entrainment of mist into the diffusion flame. As described earlier the droplet range is divided into 5 sections. The movement of the various droplet sections was analyzed by the velocity profiles. Velocity profiles (velocity component normal to the burner surface) of the various sections along with the gas phase profile have also been shown as a function of distance above the burner surface in figure 14. By comparing these profiles, the effect of droplet drag and buoyancy forces on the various droplet sections can be deduced. These results show that smaller diameter droplets (50μ) quickly follow the gas phase (small characteristic time for decrease of relative velocity) and are entrained into the flame at approximately the same rate as the oxidizer. However larger diameter droplets (150μ) tend to travel with their injection velocity and exhibit larger characteristic times for the decrease in relative velocity. For the smaller droplets the drag force exerted by the gas on these droplets is able to counterbalance the droplet weight and these droplets therefore entrain into the flame along with the oxidizer. The larger droplets are not able to counterbalance their weight with the drag force. Due to the varied characteristic times associated with the different diameter droplets it is found that the effect of injection characteristics on flame suppression are more critical for the larger diameter droplets. The smaller diameter droplet entrain most rapidly into the flame when injected in a co-flow configuration, whereas larger diameter droplets entrain at a slower rate.

3.5 Comparison of Suppressant Results to Experimental Data

Figure 15 shows the comparison between numerically computed and experimentally measured temperature profiles in a methane-air diffusion flame when steam (3% mass fraction) is added to the co-flow air. The comparison has been made at the heights of $10mm$, $30mm$ and $45mm$ above the burner. Figure 16 shows a similar comparison when water mist (3% mass fraction) was added. In general the numerically predicted profiles compare well with the experimentally measured profiles. However the comparisons become poorer as the height above the burner increases. An interesting observation from figures 15 and 16 is that water mist suppresses flame temperature more than steam does. This is due to the role played by the latent heat for water evaporation. The mechanisms of flame temperature suppression by water mist are discussed in more detail later in this section. Experimentally the injection of water mist makes the flame flicker. This results in the mixing of hot and cold regions near the flame sheet at any given distance above the burner surface. Because of flickering, it is difficult to define a steady temperature at a point whenever mist is introduced. Because the flame moves, the thermocouple encounters various regions of the flame as the thermocouple waits to make a measurement. This results in a large variation of temperature with time. The effect of flickering varies with location in the flame and also with the mist concentration. At lower heights and near the center of the flame, it is not as severe, but it becomes very severe near the edge of the flame as the plume region is approached (see figure 17).

Such changes in temperature with time at similar locations in the base case tests and in tests with nitrogen are insignificant. At each point where temperature is measured, maximum, minimum and mean values of the set of data are obtained. The experimental data in figure 16 are mean time averaged thermocouple measurements. Despite the uncertainty resulting from flame fluctuations, the comparison for the 3% mist case is good.

Figure 18 shows comparison of numerically predicted and experimentally measured temperature profiles as a function of height above the burner surface. The numerical result is the maximum temperature at a given height above the burner surface, whereas the experimental results include the maximum, mean and minimum of the time dependent temperature data. At each height above the burner surface, the time dependent profiles are experimentally measured at various points across the flame. The maximum, mean and minimum temperatures shown in figure 18 are the maximum values at a given height. The maximum and minimum temperatures at a given height thus provide an upper and lower bound. As expected the numerical results fall within the limits predicted by the experimental data. The maximum possible flame suppression was also computed using the NASA thermochemical equilibrium code [42]. As expected, the numerically observed suppression was less than the maximum possible suppression obtained from the equilibrium calculations.

3.6 Mechanisms of Flame Suppression

There are four basic mechanisms [43] involved in the extinction/suppression of flames by water mist. These include thermal cooling, oxygen displacement, fuel surface cooling and radiation attenuation. Since the focus of the present work is on gas phase diffusion flames, the effects of fuel surface cooling and radiation attenuation have been neglected. Numerical simulations were performed to examine the relative contributions of thermal cooling and oxygen displacement during water mist suppression of diffusion flames. When diffusion flames are subjected to water-mist, water droplets evaporate by absorbing energy from the flame. This effect of the latent heat of evaporation is included in the "thermal cooling" effect. Once the droplets evaporate, they produce water vapor which dilutes the oxidizer or the surrounding air flow. This oxygen displacement further suppresses the flame because of changes in rates of exothermic chemical reactions because of changes in densities of the reactants. The water vapor, due to its larger heat capacity as compared to air, can also change the specific heat of the the reactant gases resulting in further suppression of the flame. A more drastic effect of water vapor can be in the form of reduction / displacement of oxygen to a point where the flame extinguishes due to oxygen starvation. This scenario is more relevant to fires that occupy a large part of their enclosures. All these effects, other than that associated directly with the latent heat of evaporation are included in the "oxygen displacement effect".

As described earlier, numerical simulations were performed with 50μ droplets injected along with the air co-flow at a velocity of $25cm/sec$ and an initial spray injection density of $2000drops/cm^3$. These results were shown in Figure 9. This numerical simulation was repeated with zero value for the heat of evaporation to examine the relative contribution of the thermal cooling and oxygen displacement to flame suppression. Figure 19 shows temperature profiles for a) the base case methane-air diffusion flame, b) flame subjected to water mist droplets and c) flame subjected to water mist droplets but with latent heat of evaporation set to zero. As the water droplets are introduced into the flame (Case b), the flame appears to cool down significantly as compared to the base case flame (Case a). The flame also becomes taller and broader, when subjected to fine water mist. When the latent heat of evaporation is set to zero (Case c), the flame height was found

to be comparable with that of the water mist case (Case b). Figure 20 shows the temperature profiles for these three cases at four heights (25, 50, 75 and $100mm$) above the burner surface. At the heights of $25mm$ and $50mm$ above the burner surface, the base case temperature profile almost overlaps the temperature profile for the case of water mist with zero heat of evaporation. The profile for water mist with normal values of heat of evaporation shows significant suppression in flame temperature. This implies that at heights of $25mm$ and $40mm$ above the surface the principal effect of water mist is through the latent heat of evaporation and that oxygen dilution has a negligible effect on flame suppression. As one moves further above the burner surface, the effect of oxygen displacement increases. At the heights of $75mm$ and $100mm$ above the burner surface, the numerical results indicate that oxygen displacement is equally important for flame suppression as is thermal cooling [43], [44]. Our results thus indicate that the effect of oxygen dilution is more prominent in the upper part of the flame, whereas, endothermic heat exchange with the droplets play a critical role in the lower half of the diffusion flame. Figure 21 shows temperature profiles at four different heights above the burner surface for the three cases discussed in figure 19. The droplet diameter in this case was 150μ as opposed to 50μ for Figure 20. Again the results indicate that the relative contribution of the various suppression mechanism varies with height above the burner surface as well as with droplet diameter and injection velocity of the water droplets.

3.7 Effect of Droplet Diameter, Injection Density and Velocity

A series of parametric studies were performed to estimate the effect of droplet number density and droplet mass density on flame suppression and flame extinction. Figure 22 shows changes in peak temperature as a function of droplet mass density. Numerical simulations were performed with 50, 100 and 150μ droplets with varying levels of injection spray densities. The injection velocity of the droplets was unchanged in these calculations. The peak temperature observed for each simulation was mapped as a function of droplet number density as well as mass density. The profiles of peak temperature vs. droplet injection mass density indicate that as the droplet mass density increases, the flame temperature reduces until a certain critical mass density is reached beyond which point a stable flame cannot be sustained. This trend was observed for all water mist droplet diameters studied in this analysis. It is also observed that as the droplet diameter increases, the injection spray mass density required to produce the same amount of suppression also increases. Thus in a co-flow configuration, smaller diameter mist droplets result in better and more efficient suppression for the same injection mass density. The profile of peak temperature as a function of injection number density (Figure 23) show that the trends are reversed. These profiles show that larger diameter droplets produce more effective suppression for a fixed inlet injection number density. This is because when the injection number density is held fixed, larger diameter droplets result in larger amount of mass entrained into the flame as compared to smaller diameter droplets.

Figure 24 shows the centerline H_2O gas density for various spray injection densities of 50μ droplets. This figure also shows the base case centerline H_2O gas density profile. Since water mist is absent in the base case calculation, this density value is purely due to convection and diffusion of water-vapor produced during chemical reactions alone. The difference between the spray injection density profile and the base case profile gives a rough measure of the amount of H_2O gas entrained into the flame. As expected, it is found that as the spray injection density increases the amount of mist entrained into the flame also increases for a given initial droplet diameter. Figure 25 shows the centerline temperature profiles for various spray injection densities. The droplet diameter

and droplet velocity are the same as for the case shown in Figure 24. As the droplet density increases, the centerline temperature reduces and this difference in temperature represents the net suppression due to a combined effect of thermal cooling and oxygen dilution. It should be noted that temperature reduction at the centerline is negligibly small during the first 1.5 cm above the burner surface, but then increases with the height. Figure 26 shows the amount of mist entrained as a function of water mist droplet diameter. The figure clearly shows that at small heights ($10mm$) the amount of mist entrained reduces as the droplet diameter increases. Larger diameter droplets preserve their initial momentum for a longer time than the smaller diameter droplets. As a result, the larger diameter droplets take a longer time to be entrained into the flame. Figure 27 shows the amount of mist entrained at the centerline as a function of spray injection flux density for three initial droplet diameters and at three different heights above the burner surface. We observe that the amount of entrainment increases linearly with spray injection flux density ($\dot{m}_{H_2O}/\dot{m}_F$). Droplet entrainment increases with height above the burner surface for a given droplet diameter. Figure 27 further shows the impact of droplet diameter on entrainment rate above the burner surface. It is clearly shown that the smaller diameter droplets entrain more readily into the flame whereas larger diameter droplets entrain at a smaller rate, for a given spray injection density and at a given height above the burner surface. This result is strictly valid only when the mist is introduced parallel to the air-flow.

The net suppression due to water mist and the impact of droplet diameter, injection velocity and spray density have been summarized in Figure 28. The abcissa of this figure shows the net amount of water mist injected per unit mass flow rate of fuel, whereas the ordinate is a ratio of the integrated heat release in the computational domain with water mist (ΔH_T) to the integrated value without water mist (ΔH_o). This ratio therefore represents a net integrated measure of the suppression of a flame. Efficient design of water mist systems aims at obtaining the maximum amount of suppression with the minimum amount of water mist added to system, that is to minimize the value of the abcissa and the ordinate. Results for various droplet diameter (50, 100 and 150μ) with various injection velocities show the net suppression that is observed for the various cases. The ratio of the water supply rate to the fuel rate required for extinction of the diffusion flame is approximately 10 for 50μ droplets and increases to 40 for 150μ droplets. For each droplet diameter, the net suppression increases with spray density. Figure 28 also shows three cases in which the spray injection velocity is increased from $25cm/sec$ to $500cm/sec$. The droplet diameter for these cases is 150μ. As the spray velocity increases, we find that net suppression reduces for a given mist flux density. Overall our results indicate that for the co-flow configuration, smaller diameter droplets produce maximum suppression for the minimum spray mass density.

4. CONCLUSIONS

A numerical model has been developed to study the combustion of methane-air diffusion flames and their inhibition by water mist. Both the gas phase and the droplet phase flows are described by equations in the Eulerian form. The complete set of unsteady compressible Navier Stokes equations are solved for studying methane -air diffusion flames stabilized above Wolfhard Parker burners. A sectional approach has been adopted in which the entire droplet size domain is divided into a few sections and an integral quantity representing each section is conserved. The model has been validated by comparing temperature profiles with experimental measurements. The model has been used to understand the impact of droplet diameter, spray velocity and injection characteristics on mist entrainment into the diffusion flame and flame suppression. Numerical simulations have been

performed to identify the relative contribution of the various suppression mechanisms. Our results indicate that smaller droplets exhibit smaller characteristic time for decrease in relative velocity, with respect to the gas phase, and therefore entrain most rapidly into the diffusion flame. Hence, for the co-flow injection case, smaller diameter droplets produce maximum flame suppression for a fixed amount of injection spray density. The ratio of water supply rate to the fuel supply rate required for extinguishment, reduces with decreasing droplet size for laboratory flames.

Additional studies are being pursued with different mist injection configurations such as side injection, top injection or injection at an angle to the co-flow to further optimize the various water mist injection characteristics for flame suppression. The net suppression (ΔH_T) for the various mist injection configurations will be computed and presented in a form similar to the one shown in Figure 28. The suppression of non-symmetric flames when subjected to side injection of fine water mist is being investigated using numerical simulations in which the symmetry condition is no longer enforced. These studies would help in optimizing spray injection characteristics for flame suppression. Another part of this research is directed toward simulating methanol or heptane liquid pool fires and simulating the changes in burning rates when subjected to fine water mist droplets. The effect of droplet diameter, spray injection velocity and mist density on methanol burning rates will be investigated. The effect of gas velocity on droplet entrainment into the diffusion flame needs to be studied further. Instead of the eulerian approach used for studying droplet evaporation, a lagrangian approach for tracking the individual droplets might also yield useful information regarding the movement of the droplets in a diffusion flame flow field. New improved models for studying the radiation attenuation of fine water mist are also required.

5. ACKNOWLEDGEMENT

6. REFERENCES

1. Evans, D. D., "Control of Blowout Fires with Water Sprays," Technology Assessment and Research Programs for Offshore Minerals Operations, OCS Report MMS 84-0001, U.S. Department of the Interior Minerals Management Service, 1984.

2. McCaffrey, B.J., "Jet Diffusion Flame Characteristics and the Effects of Water Spray," Comb. Sci. and Tech., 40, 1984, pp. 107-136.

3. McCaffrey, B.J., "Momentum Diffusion Flame Characteristics and the Effects of Water Spray," Combust. Sci. and Tech., 1989, Vol. 63, pp.315-335.

4. Evans, D.D. and Pfenning, D., "Water Sprays Suppress Gas-well Blowout Fires," Oil and Gas Journal, 8, 1985, pp. 80-86.

5. Holmsted, G. "Extinction Mechanisms of Water Mist: Water Mist Instead of Halon?," International Conference on Water Mist Fire Suppression Systems, Boras, Sweden, 1993.

6. Rashbash, D.J., " The Extinction of Fire with Plain Water: A Review," Fire Safety Science, 1986, pp. 1145-1163.

7. Tatem, P.A., Beyler, C.L., DiNenno, P.J., Budnick, E.K., Back, G.G. and Younis, S.E., "A Review of Water Mist Technology for Fire Suppression," NRL/MR/6180-94-7624, Naval Research Laboratory, 1994.

8. Rashbash, D.J., Rogowski, Z.W. and Stark, G.W.V., "Mechanism of Extinction of Liquid Fires by Water Sprays," Comb. and Flame, Vol. 4, pp.223, 1960.

9. Rashbash, D.J. and Rogowski, Z.W., "Extinction of Fires in Liquids by Cooling with Water Sprays," Comb. and Flame, Vol. 1, 1957.

10. McGee, R.S., and Reitz, R.D., "Extinguishment of Radiation Augmented Plastic Fires by Water Sprays," Fifteenth Symposium (International) on Combustion, The Combustion Institute, 1974, pp. 337-347.

11. Tamanini, F., "A Study of the Extinguishment of Vertical Wood Slabs in Self-sustained Burning by Water Spray Application," Comb. Sci. and Tech., 14, 1976, pp. 17-23.

12. Tamanini, F., " The Application of Water Sprays to the Extinguishment of Crib Fires," Comb. Sci. and Tech., 14, 1976, pp.17-23.

13. Downie, B., Polymeropoulos C. and Gogos, G., "Interaction of a Water Mist with a Buoyant Methane Diffusion Flame," Fire Safety Journal, 24, 1995, pp. 359-381.

14. Beyler, C.L.,"A Unified Model of Fire Suppression," Journal of Fire Protection Engineering, 4, 1992, pp. 5-16.

15. Seshadri, K., "Structure and Extinction of Laminar Diffusion Flames Above Condensed fuels with Water and Nitrogen," Comb. and Flame, 33, 1978, pp. 197-215.

16. Lentati, A.M. and Chelliah, H.K., "The Dynamics of Water Droplets in a Counterflow Field and its Effects on Flame Extinction," Proceeding of the Fall Technical Meeting, The Eastern States Section of the Combustion Institute, p. 281, 1996.

17. Mell, W.E., Baum, H.R. and McGratten, K., "Simulation of Fires with Radiative Heat Transfer," 2nd International Conference on Fire Research and Engineering, August 1997.

18. McGratten, K. and Stroup, D., "Sprinkler, Vent and Draft Curtain Interaction - Experiment and Computer Simulation," 2nd International Conference on Fire Research and Engineering, August 1997.

19. Nam, S., "Parametric Study with a Computational Model Simulating Interaction Between Fire Plume and Sprinkler Spray," Annual Conference on Fire Research, 1996.

20. Hung, L.S., Yao, S.C., "Numerical Studies on the Deposition and Transport of Water Mist Normal to a Horizontal Plate," Annual Conference on Fire Research and Engineering, August, 1997.

21. Ewing, C.T., Faith, F.R., Hughes, J.T. and Carhart, H.W., " Flame Extinguishment Properties of Dry Chemicals," Fire Technology, 25, 2, 1989.

22. Ewing, C.T., Hughes, J.T., and Carhart, H.W., " The Extinction of Hydrocarbon Flames Based on the Heat Absorption Processes which Occur in Them," Fire and Materials, 8, 3, 1984.

23. Chen, N.H. and Rogg, B., " Bifurcations in Two-phase Flames," Instabilities in Multiphase flows, G. Gouesbet and A. Berlemont (ed.), Plenum Press, NY 1993, pp. 149-160.

24. Chen, N.H., Rogg, B., and Bray, K.N.C., " Modelling Laminar Two-phase Counterflow Flames with Detailed Chemistry and Transport," Twenty-fourth Symposium (International) on Combustion, The Combustion Institute, 1992, pp. 1513-1521.

25. Atreya, A., Crompton, T. and Suh, J., "An Experimental and Theoretical Study of Mechanisms of Fire Suppression by Water," NIST Annual Conference for Fire Research, pp. 67, NISTIR 5499, 1994.

26. Blevin, L.B., and Roby, R.J., "Effects of High Levels of Steam Addition on NO_x Reduction in Laminar Opposed Flow Diffusion Flames," Mechanical Engineering, Virginia Polytechnic Institute and State University, Blacksburg, VA, 1992.

27. Williams, F.A., Combustion Theory, 1985, Addison-Wesley Publishing Co., Inc., New York.

28. Kuo, K.K., Fundamentals of Combustion, 1986, Wiley, NY.

29. Prasad, K., Li, C., Kailasanath, K., Ndubizu, C., Gopal, R. and Tatem, P.A., "Numerical Modeling of Water Mist Suppression of Methane-Air Diffusion Flames," submitted, Combustion Science and Technology, 1997.

30. Kailasanath, K., Oran, E.S. and Boris, J.P., "A One-Dimensional Time Dependent Model for Flame Initiation, Propagation, and Quenching," NRL Memorandum Report 4910, Naval Research Laboratory, 1982.

31. Kee, R.J., Dixon-Lewis, G., Warnatz, J., Coltrin, M.E. and Miller, J.A., "A Fortran Computer Code Package for the Evaluation of Gas-Phase Multicomponent Transport Properties," SAND86-8246, Sandia National Laboratory, 1986.

32. Wilke, C. R., "A Viscosity Equation for Gas Mixtures," J. Chem. Phys., 18:517, 1950.

33. Westbrook, C. K. and Dryer, F. L., "Simplified Reaction Mechanism for the Oxidation of Hydrocarbon Fuels in Flames," Comb. Sci. and Tech., Vol. 27, pp. 31-43, 1981.

34. Sirignano, W.A., "Fuel Droplet Vaporization And Spray Combustion Theory," Prog. Energy Combust. Sci., 1983, Vol. 9, pp. 291-323.

35. Faeth, G.M., "Current Status of Droplet And Liquid Combustion," Prog. Energy Combust. Sci., Vol. 3, pp. 191-224, 1977.

36. Tambour, Y., "Vaporization of Polydisperse Fuel Sprays in a Laminar Boundary Layer Flow: A Sectional Approach," Comb. and Flame, 58:103-114, 1984.

37. Tambour, Y., "A Lagrangian Sectional Approach for Simulation of Droplet Size Distribution of Vaporizing Fuel Sprays in a Turbulent Jet," Comb. and Flame, 60: 15-28, 1985.

38. Silverman, I., Ph. D. Thesis, private communication, 1996.

39. Patnaik, G., Laskey, K.J., Kailasanath, K., Oran, E.S. and Brun, T.A., "FLIC - A Detailed Two-Dimensional Flame Model," NRL Memorandum Report 6555, 1989.

40. Ellzey, J.L., Laskey, K.J. and Oran, E.S., "A Study of Confined Diffusion Flame," NRL Memorandum Report 6704, 1990.

41. Boris, J.P., and Book, D.L., "Solution of the Continuity Equation by the Method of Flux-Corrected Transport," Methods in Computational Physics, 16:85-129, 1976.

42. Gordon, S. and McBride, B.J., " Computer Program for Calculation of Complex Chemical Equilibrium Compositions and Applications," NASA Reference Publication 1311, Lewis Research Center, Cleveland, OH.

43. Prasad,K., Li, C., Kailasanath, K., Ndubizu, C., Ananth, R., Tatem, P.A., "Water Mist Suppression of Methane-Air Diffusion Flames," 1996 Fall Technical Meeting, The Eastern States Section of the Combustion Institute, pp. 277, Hilton Head, South Carolina.

44. Li, C., Prasad, K. and Kailasanath, K., "Numerical Study on Water Mist Suppression of Methane-Air Diffusion Flame," NIST Annual Conference on Fire Research, NISTIR 5904, pp. 27, Gaithersburg, 1996.

Fig. 1. Schematic diagram of a 2-Dimensional Wolfhard - Parker diffusion flame burner, showing burner geometry. The burner has been modified to introduce mist into the air co-flow through mist generation chambers located next to the oxidizer channel. A fraction of the mist generated in this chamber is entrained into the air stream and interacts with the diffusion flame.

Methane-Air Diffusion Flames
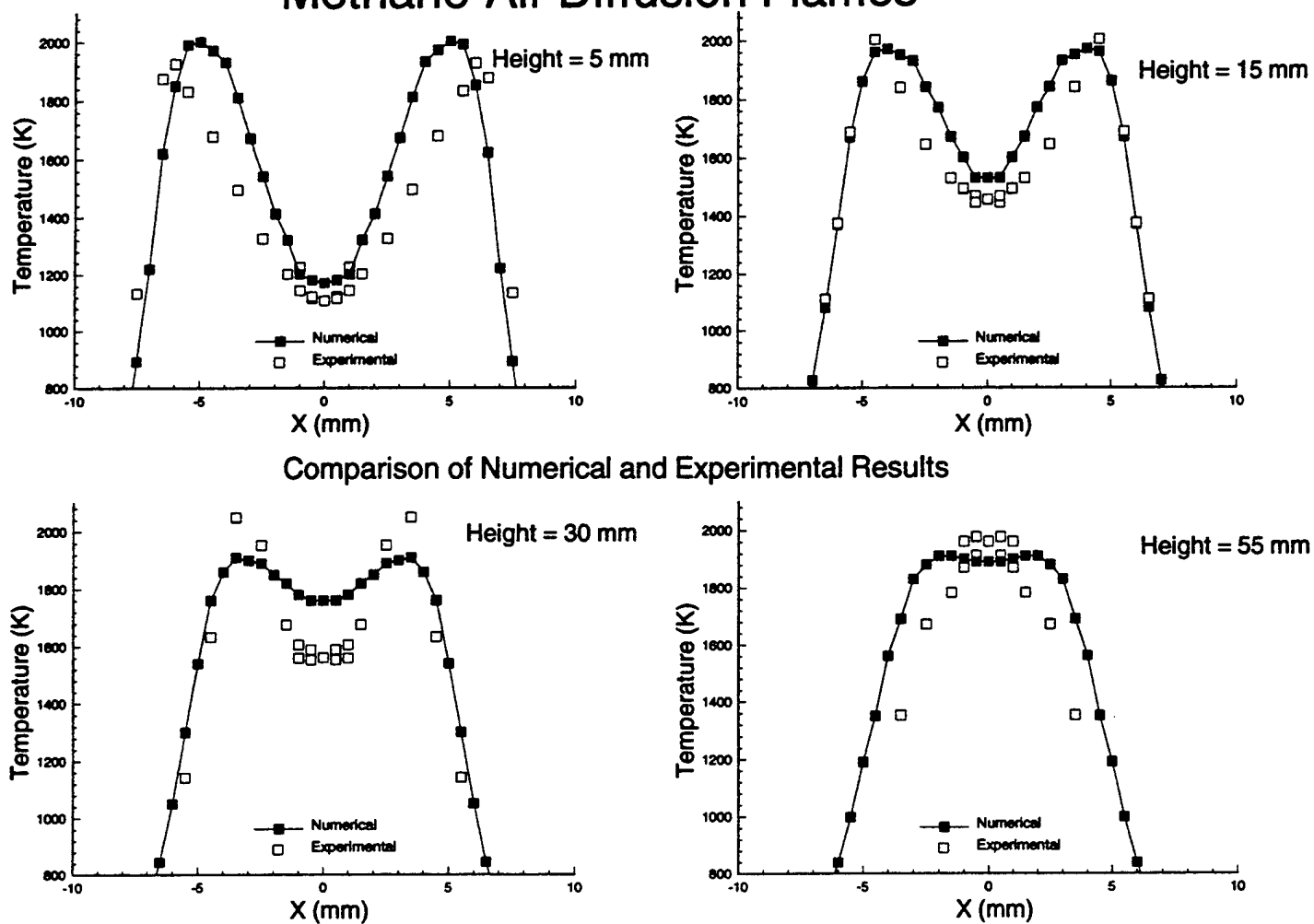
Fig. 2. Comparison of numerical and experimental results for base case $CH_4 - Air$ diffusion flame. Numerically computed temperature profiles are compared with thermocouple temperature measurements at a height of 5, 15, 30 and 55 mm above the burner surface.

Methane-Air Diffusion Flame (18 %O_2, 82 % N_2)

Comparison of Numerical and Experimental Results
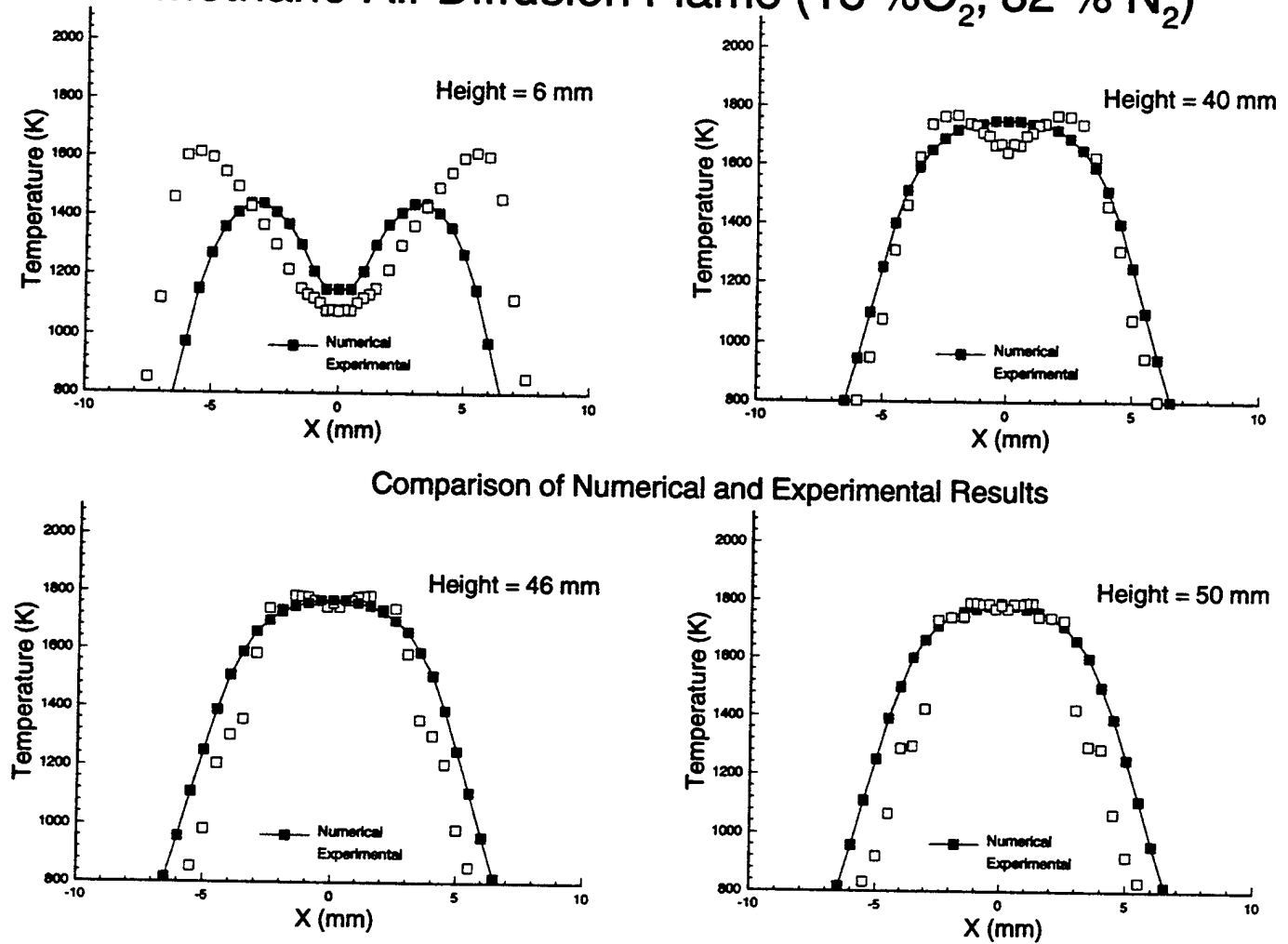
Fig. 3. Comparison of numerical and experimental results for CH_4 and 18.2%O_2, 81.8%N_2 diffusion flame. Numerically computed temperature profiles are compared with thermocouple temperature measurements at a height of 6, 40, 46 and 50 mm above the burner surface.

Methane - Air Diffusion Flames (16 %O₂, 84 % N₂)
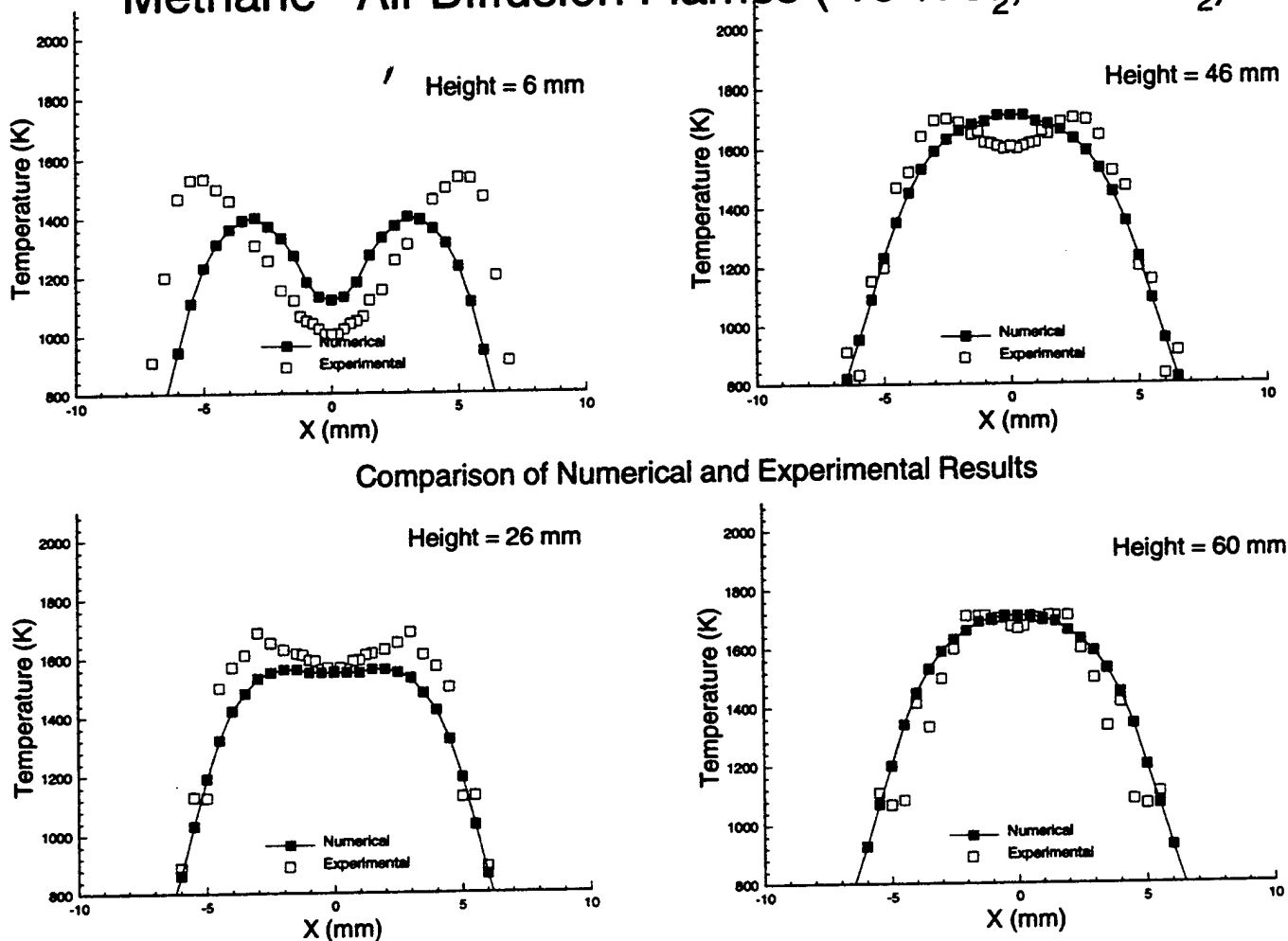
Fig. 4. Comparison of numerical and experimental results for CH_4 and $16.5\%O_2, 83.5\%N_2$ diffusion flame. Numerically computed temperature profiles are compared with thermocouple temperature measurements at a height of 6, 26, 46 and 60 mm above the burner surface.
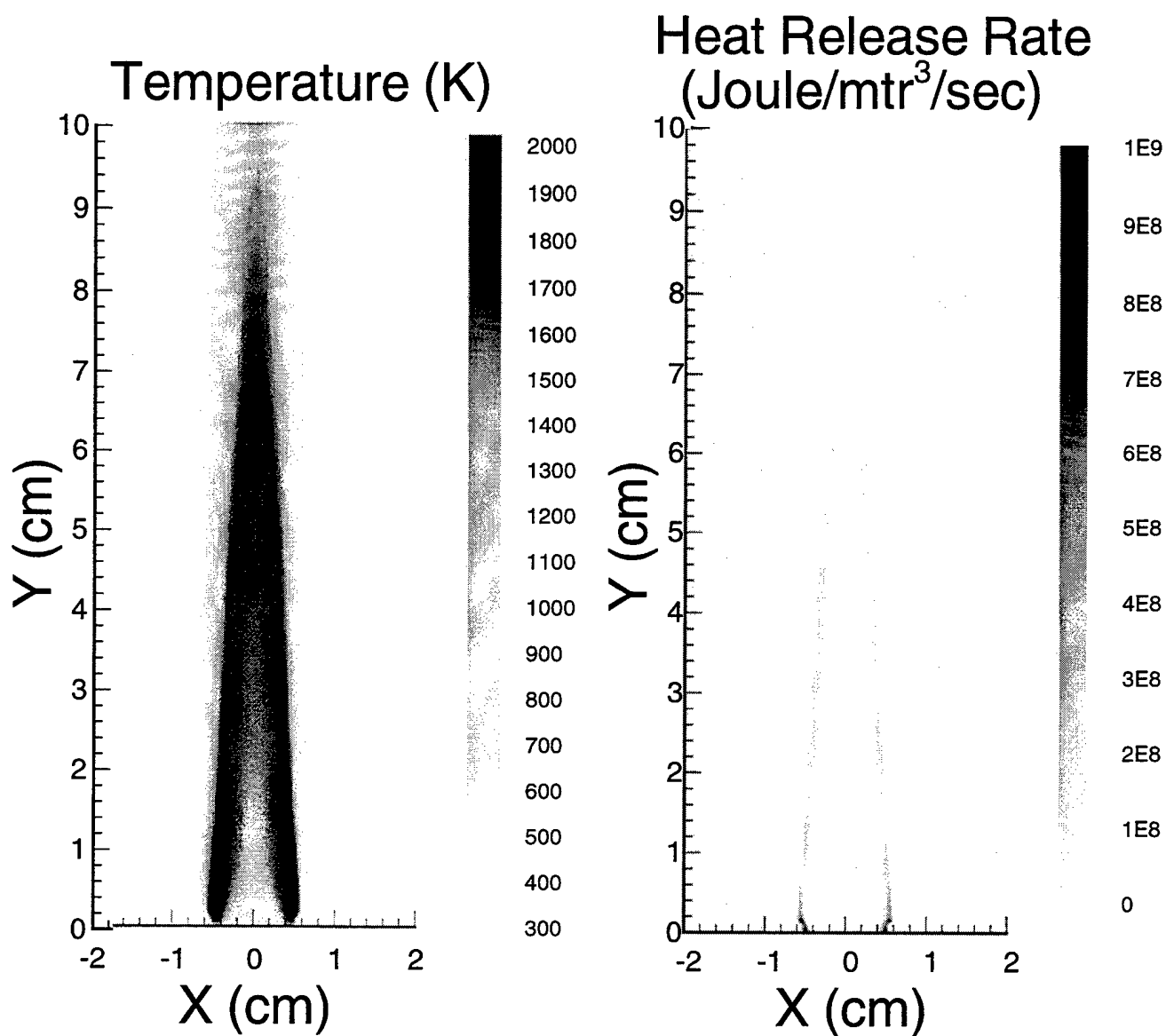
Fig. 5. Contours of temperature and heat release rate over a $CH_4 - Air$ diffusion flame burner. The fuel jet velocity is $2.81cm/sec$ and air jet velocity is $25.87cm/sec$. The flame height is approximately $7cm$ and the maximum flame temperature is $1970K$. The heat release rate profile shows the region of exothermic chemical activity above the burner surface.
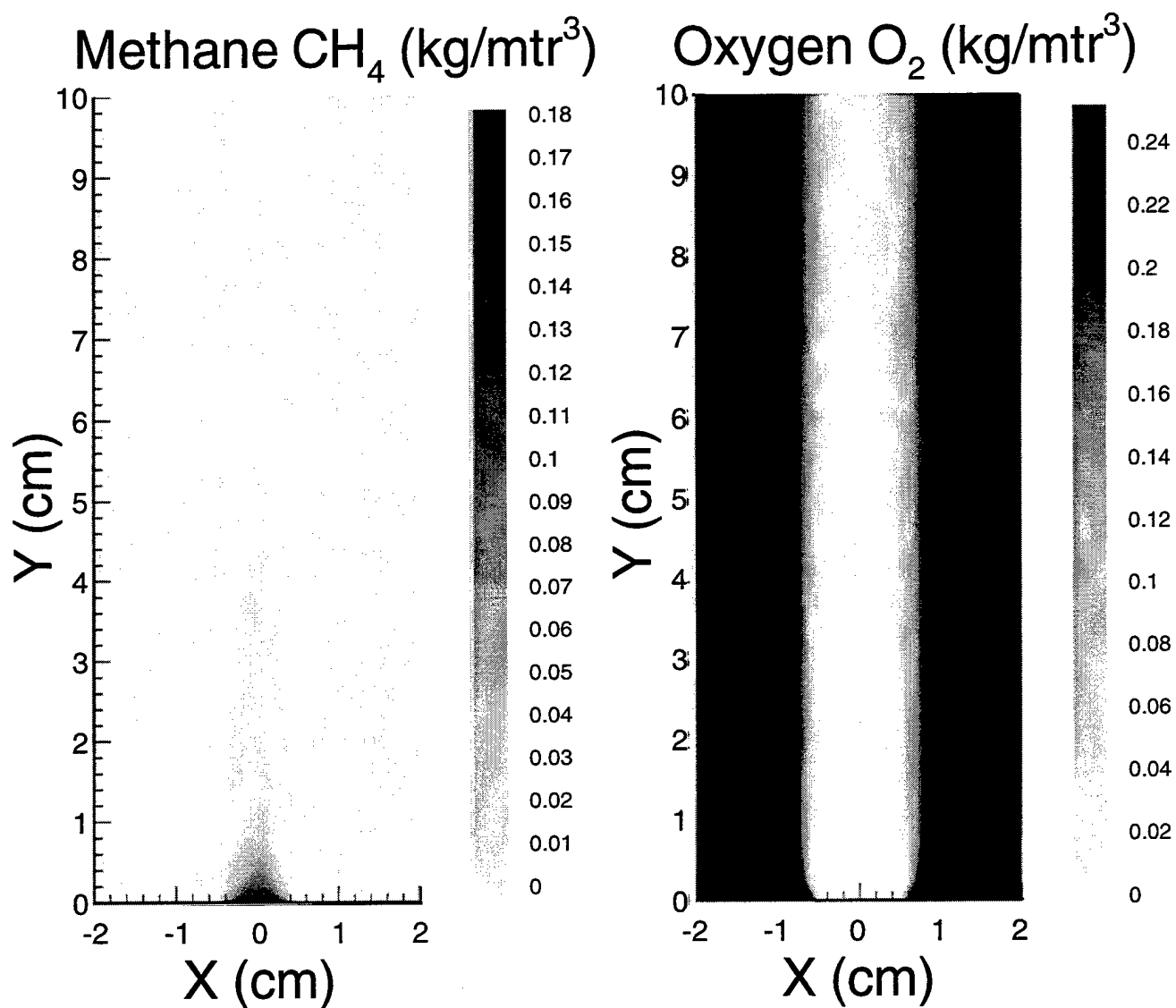
Fig. 6. Contours of methane CH_4 and oxygen O_2 density above a $CH_4 - Air$ diffusion flame burner. The fuel jet velocity is $2.81cm/sec$ and air jet velocity is $25.87cm/sec$. These calculations are performed using a single step arrhenius chemistry to study methane-air combustion.
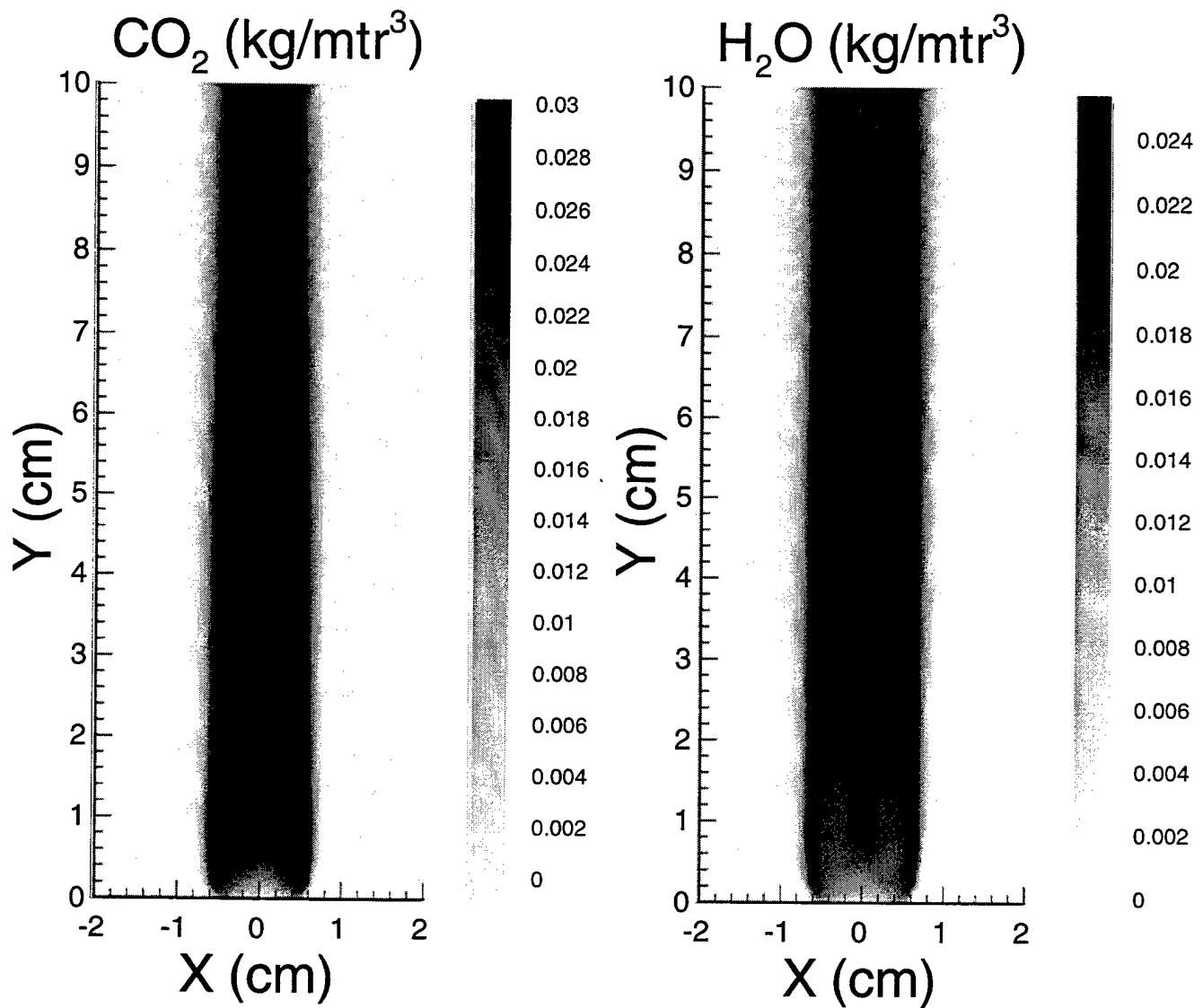
Fig. 7. Contours of product species carbon-di-oxide CO_2 and water vapor H_2O density above a $CH_4 - Air$ diffusion flame burner. The fuel jet velocity is $2.81 cm/sec$ and air jet velocity is $25.87 cm/sec$. These calculations are performed using a single step arrhenius chemistry to describe methane-air combustion.
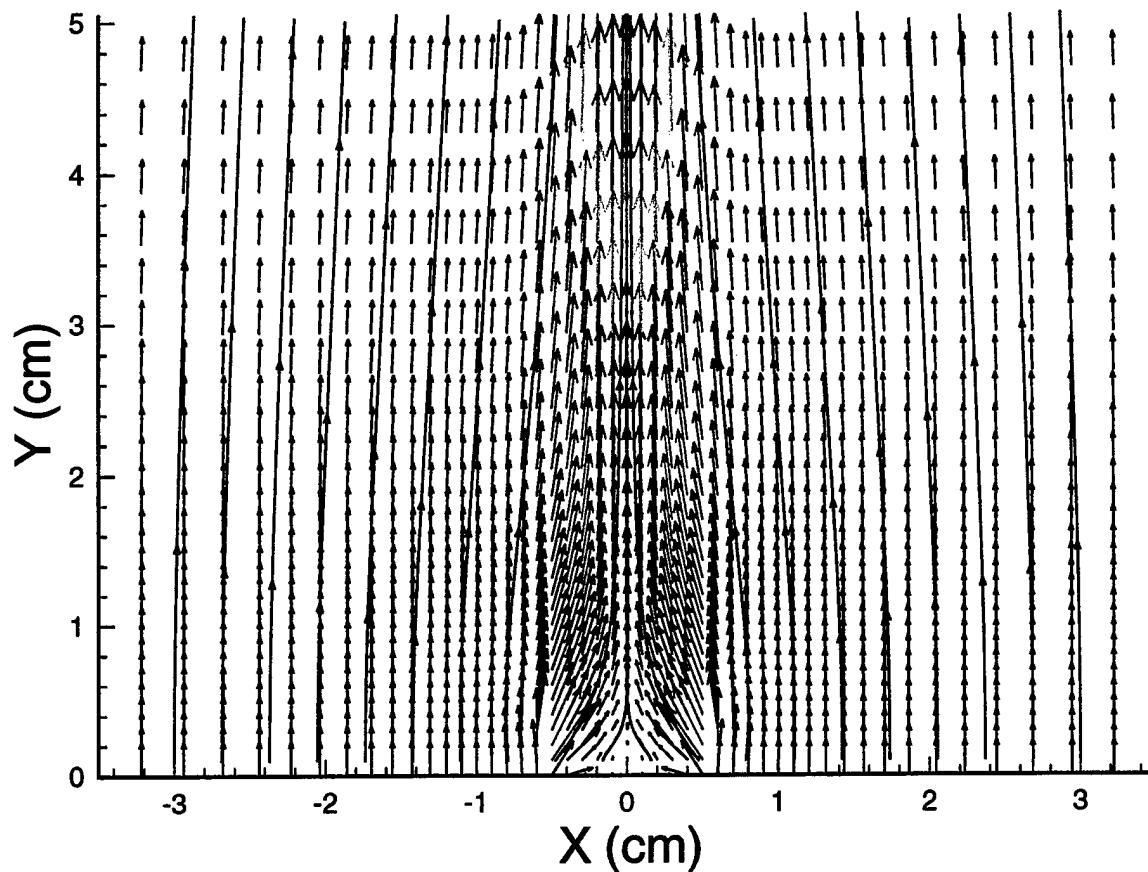
Fig. 8. Velocity vectors and stream line pattern during methane-air combustion above a Wolfhard Parker diffusion flame burner. The velocity vectors have been color coded with red showing the highest gas speed and blue showing the lowest gas velocity. The streamline pattern (black) clearly indicate the entrainment of oxidizer along with the suppressants into the diffusion flame. The fuel jet velocity is $2.81cm/sec$ and air jet velocity is $25.87cm/sec$.
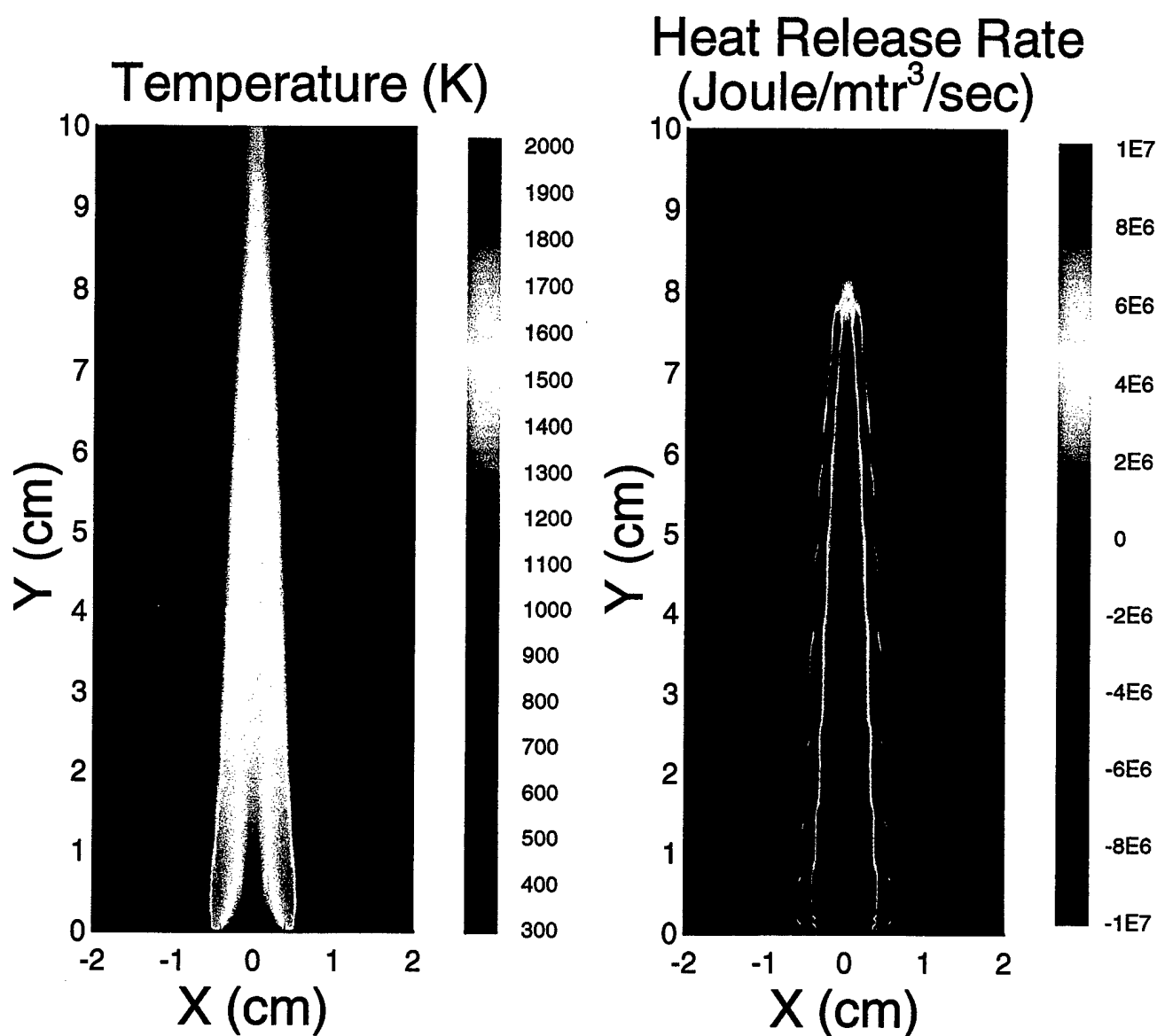
Fig. 9. Suppression of diffusion flames subjected to 50μ diameter fine water mist droplets injected with a velocity of $25cm/sec$ into the air flow. Figure shows reduction in flame temperature and heat release rate profiles. The temperature and heat release rate profiles indicate an increase in flame height and flame suppression due to sub-extinguishing application rates of water mist. The heat release rate profile also indicates the presence of an endothermic heat release profile (-ve values) showing the approximate location of evaporation of the droplets.
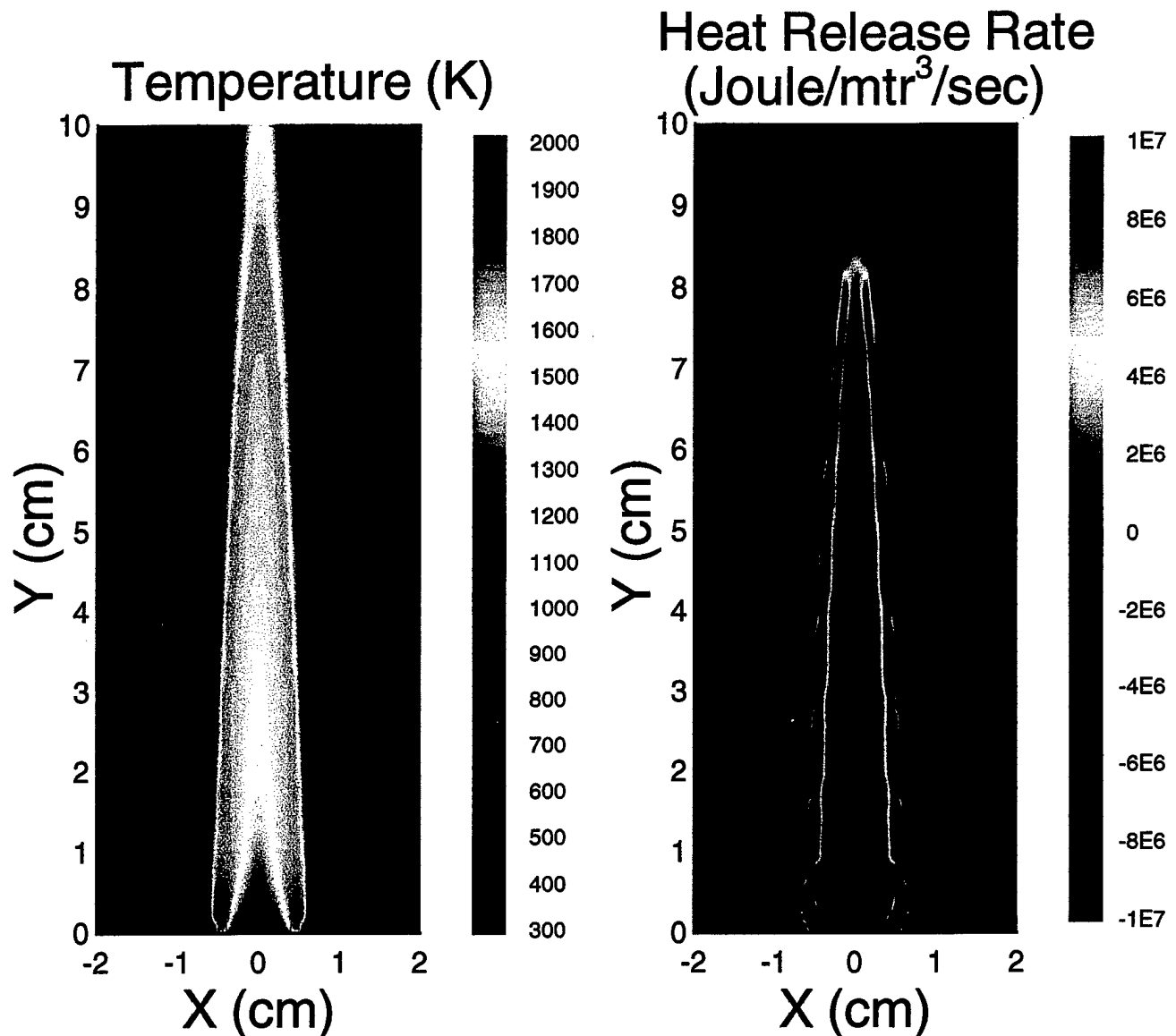
Fig. 10. Suppression of diffusion flames subjected to 150μ diameter fine water mist droplets injected with a velocity of 250cm/sec into the air flow. Figure shows reductions in flame temperature and changes to the heat release rate profile as compared to the base case. The temperature and heat release rate profiles indicate an increase in flame height and flame suppression due to the sub-extinguishing application rates of water mist. The heat release rate profile also indicates the presence of an endothermic heat release profile (-ve values) showing the approximate location of evaporation of the droplets.
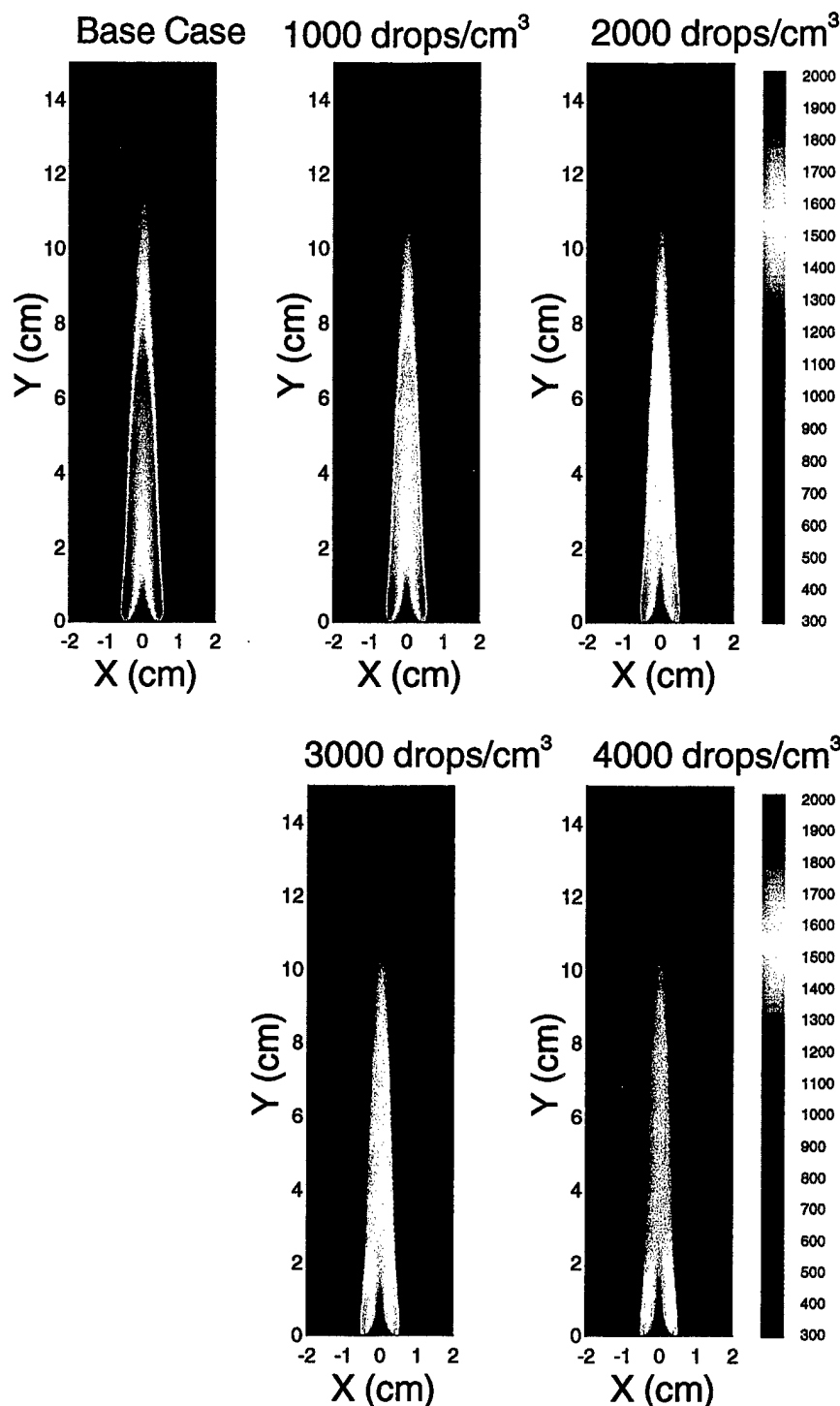
Fig. 11. Suppression of diffusion flames subjected to 50μ water mist droplets. Figure shows temperature contours for various spray injection densities of $1000, 2000, 3000$ and $4000 drops/cm^3$. These droplets are injected along with the air with an initial injection velocity of $25cm/sec$. Also shown are the base case profiles indicating various levels of suppression.

The flame height increases from $7cm$ for the base case to $11cm$ for injection of $4000drops/cm^3$ and the flame temperature decreases from $1970K$ to $1695K$.
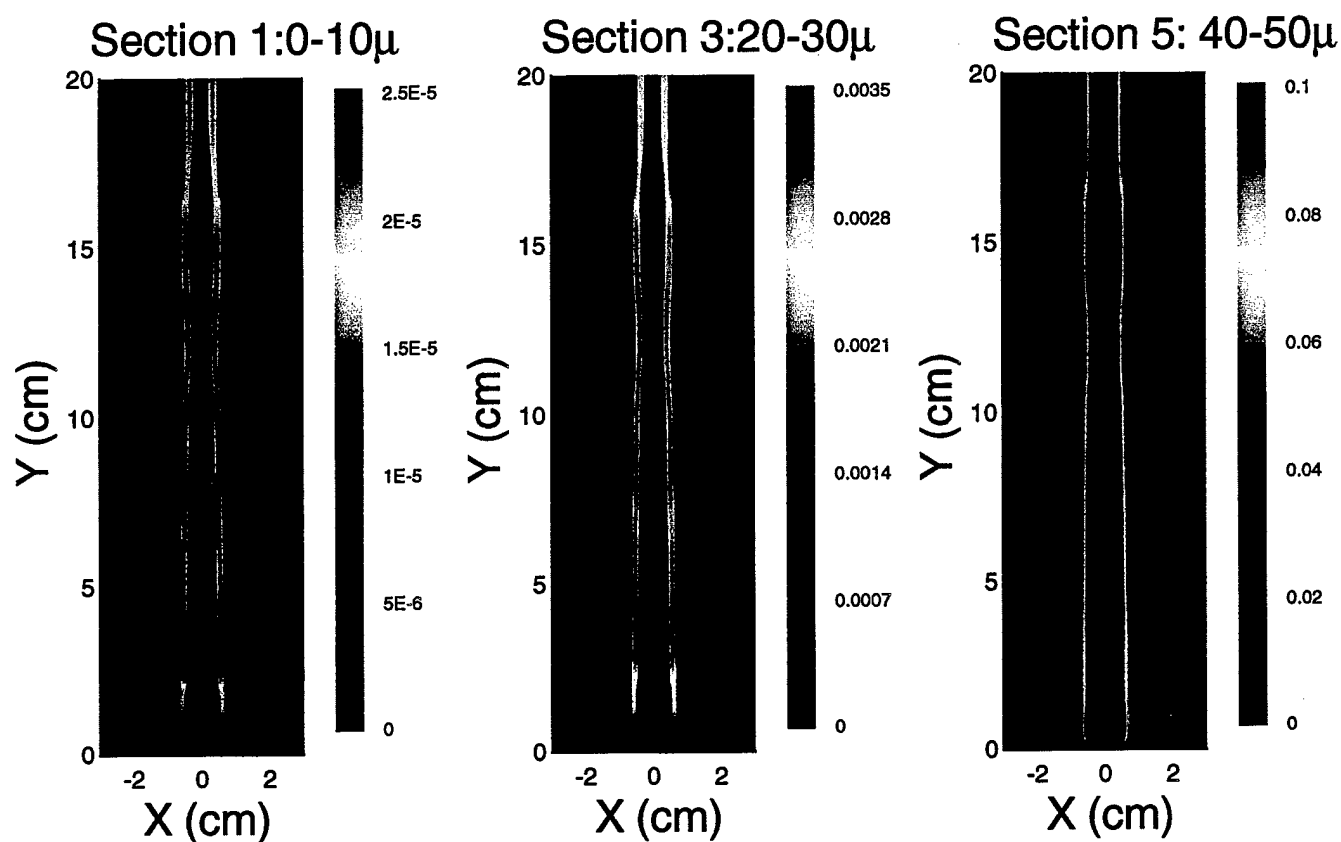
Fig. 12. Sectional droplet density contours for the injection of 50μ water mist droplets along with the air co-flow. The droplets are divided into 5 sections as follows: $0 - 10\mu$, $10 - 20\mu$, $20 - 30\mu$, $30 - 40\mu$ and $40 - 50\mu$. Droplet section densities for three of the five sections have been shown to illustrate the location of maximum density and position where these droplets evaporate to form smaller and smaller droplets (sections).

Section 1: 0 -30 μ

Section 3: 60 -90μ

Section 5: 120-150μ
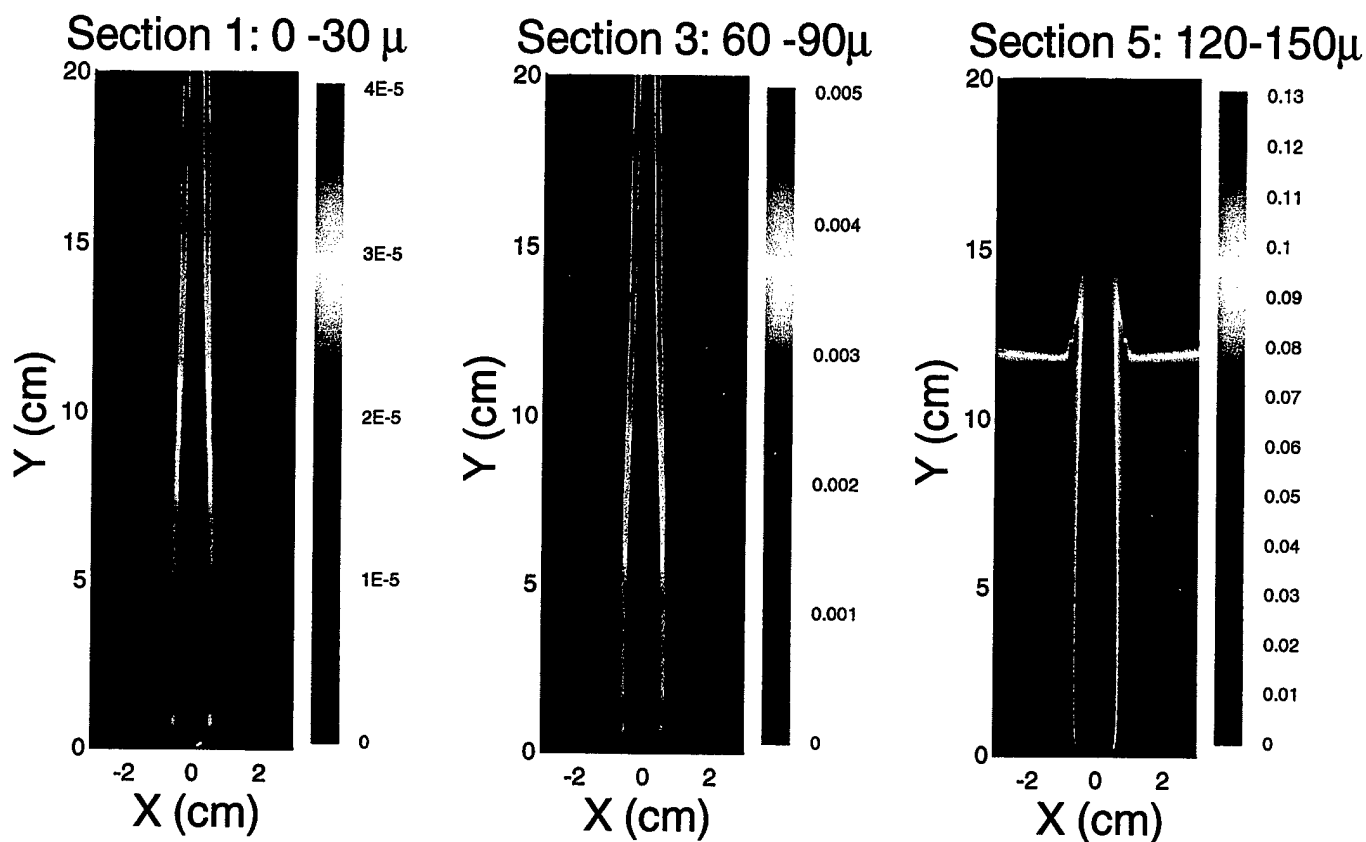
Fig. 13. Sectional droplet density contours for the injection of 150μ water mist droplets along with the air co-flow. The droplets are divided into 5 sections as follows: $0 - 30\mu$, $30 - 60\mu$, $60 - 90\mu$, $90 - 120\mu$ and $120 - 150\mu$. Droplet section densities for three of the five sections have been shown to illustrate the location of maximum density and position where these droplets evaporate to form smaller and smaller droplets (sections).
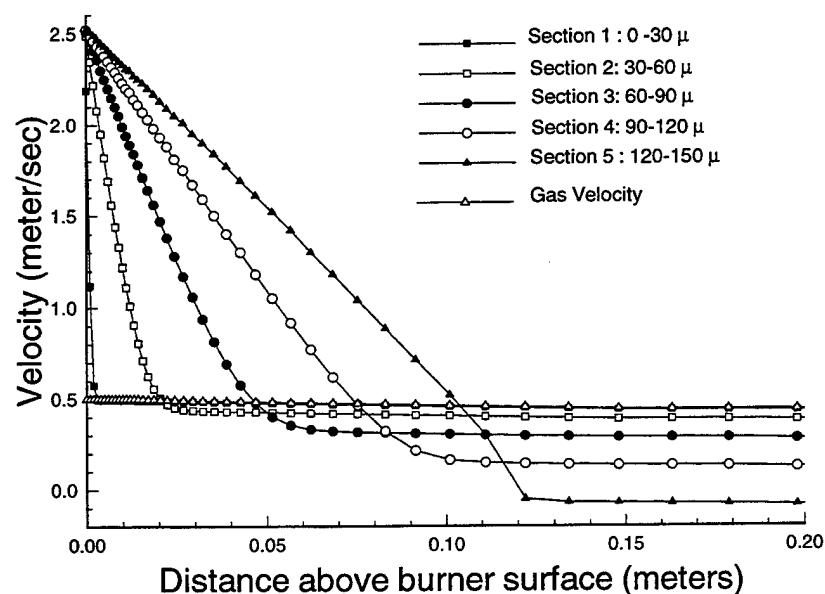
Fig. 14. Velocity profiles of the various sections have been shown as a function of distance above the burner surface for the injection of 50μ water droplets. The velocity component shown is normal to the burner surface. The droplets are divided into 5 sections as follows: $0 - 30\mu$, $30 - 60\mu$, $60 - 90\mu$, $90 - 120\mu$ and $120 - 150\mu$.

Also shown are the gas phase profiles indicating the effect of droplet drag and buoyancy forces on various droplet sections. This figure illustrates the different characteristic times for reduction of relative velocity for the various droplet diameters.
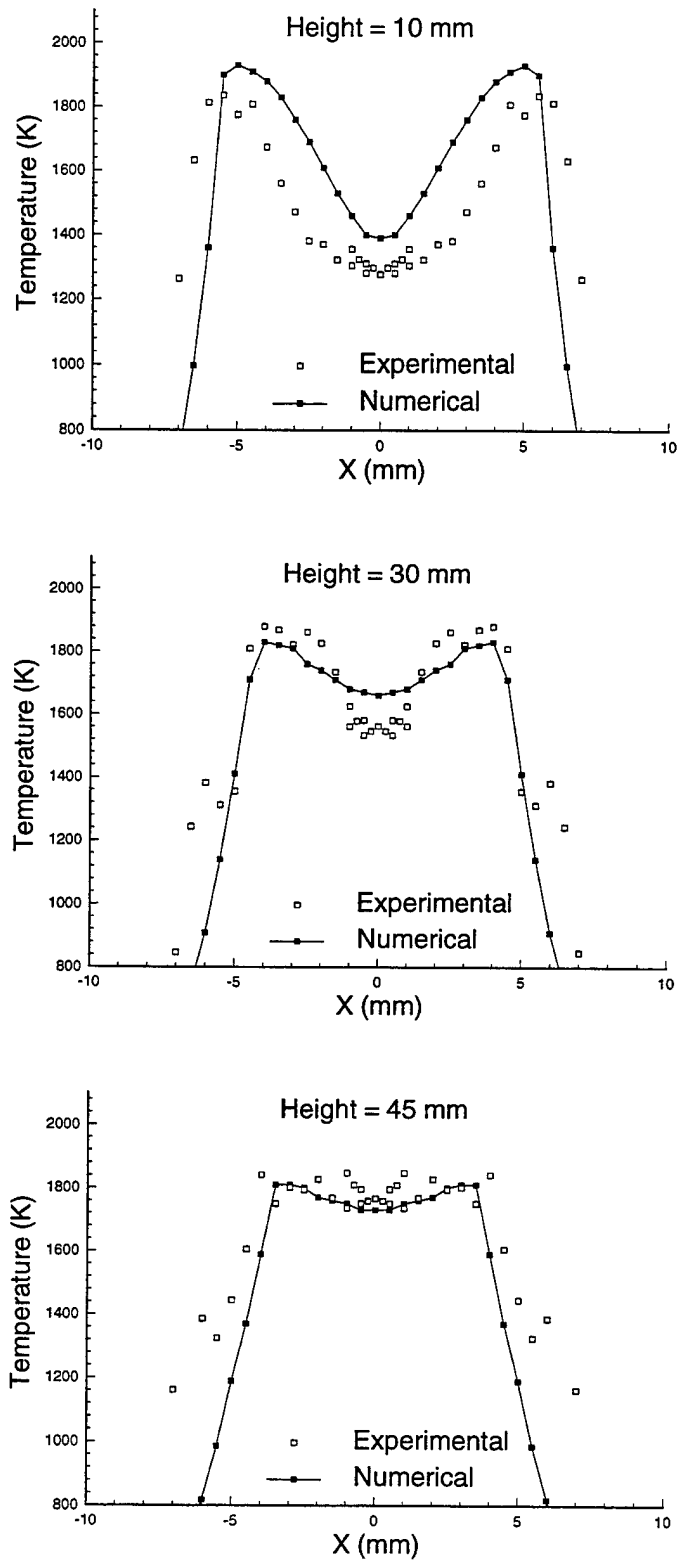
Fig. 15. Comparison of numerically computed and experimentally measured temperature profiles at a height of $10mm$, $30mm$ and $45mm$ above the burner surface with injection of 3% mass fraction steam along with the air co-flow.
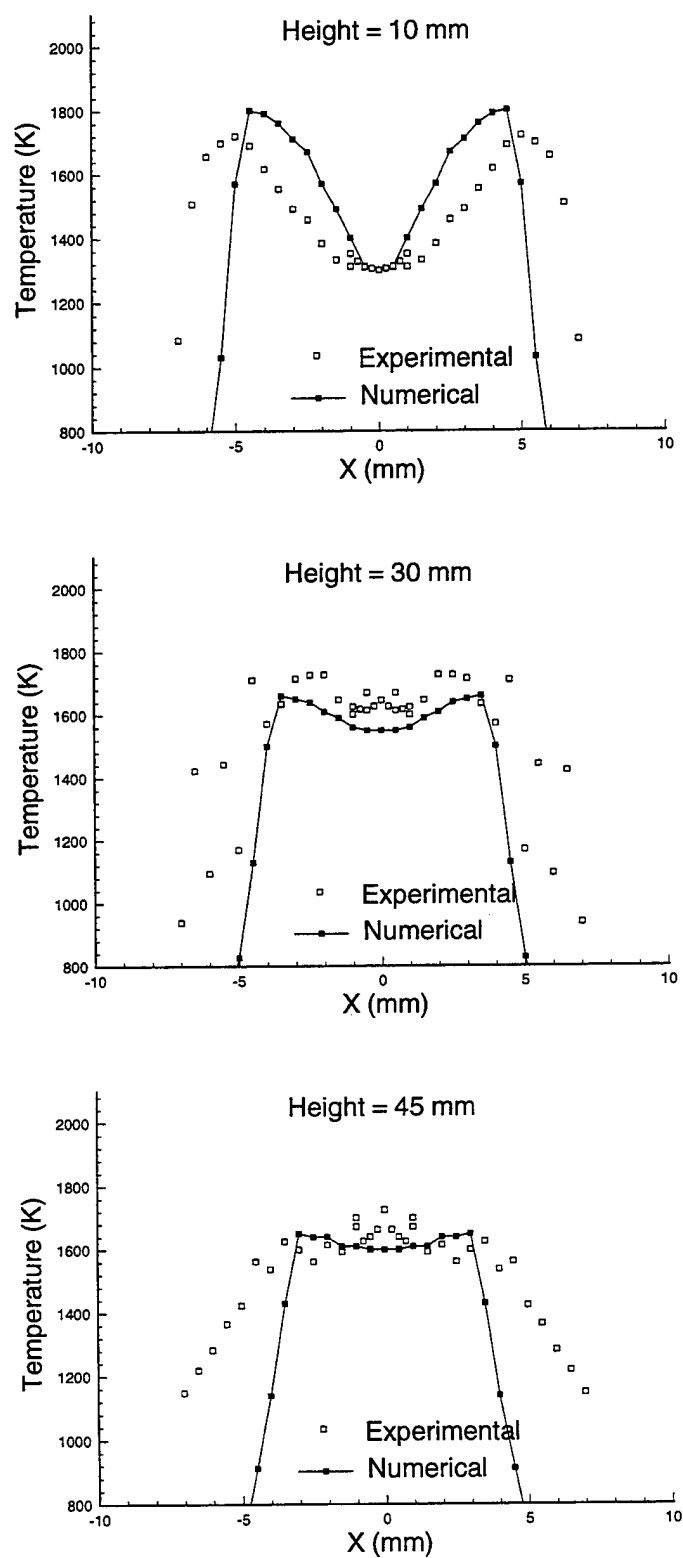
Fig. 16. Comparison of numerically computed and experimentally measured temperature profiles at a height of 10*mm*, 30*mm* and 45*mm* above a burner surface for injection of 3% mass fraction water mist droplet of 50μ diameter.

a) Base Case Methane-Air Diffusion Flame
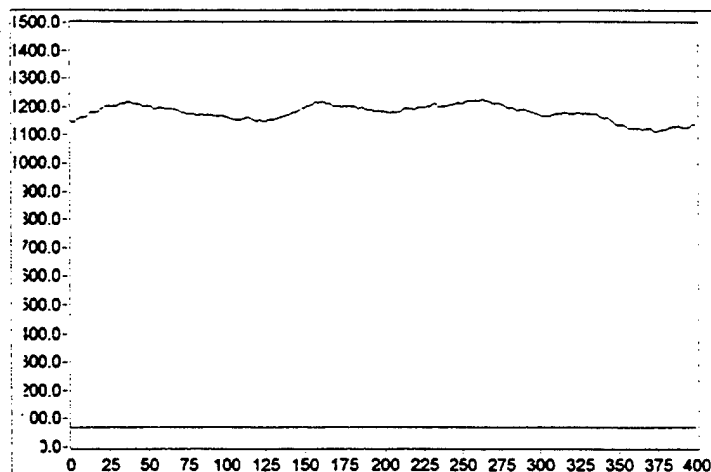
Location: $(5mm, 30mm)$ Location: $(0mm, 10mm)$
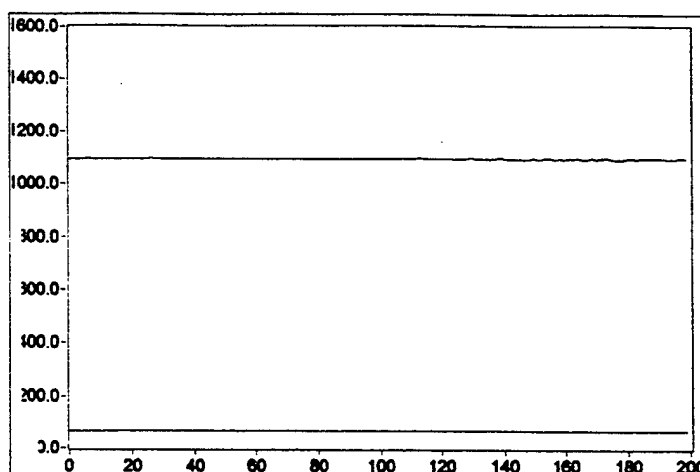
b) Diffusion Flame with Water Mist
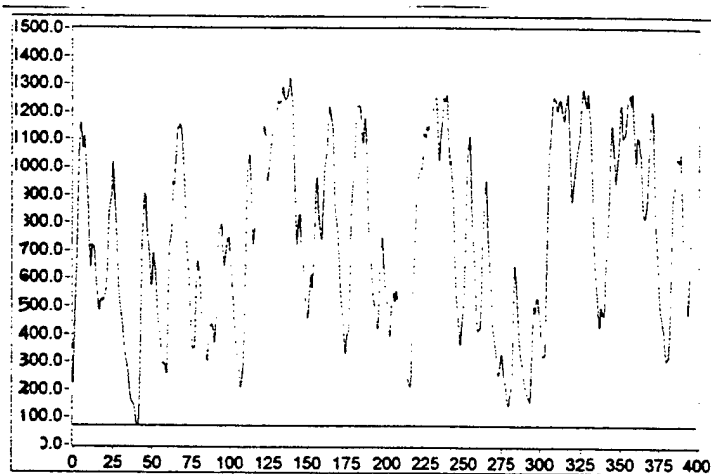
Location: $(5mm, 30mm)$ Location: $(0mm, 10mm)$
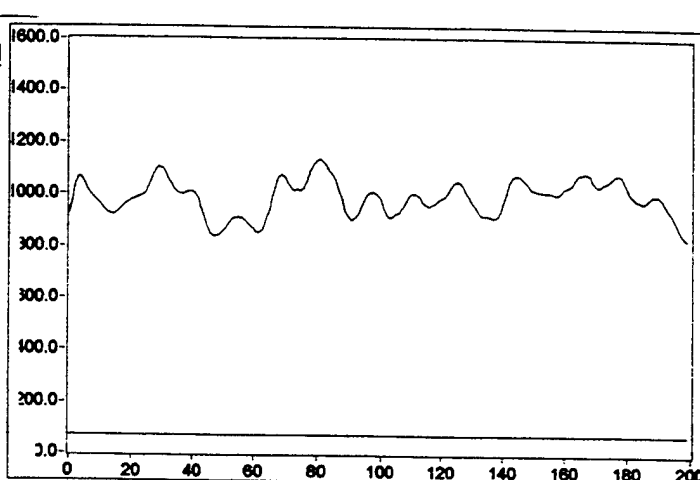
Fig. 17. Experimentally measured temperature-time history at two different points (5mm,30mm) and (0mm,10mm) for the a) base case methane-air diffusion flame, b) diffusion flame subjected to 3% mass fraction, 50μ water mist droplets injected along with the air co-flow. Figure illustrates that the diffusion flame subjected to water mist fluctuates rapidly and is shown by the changes in thermocouple temperature measurements.
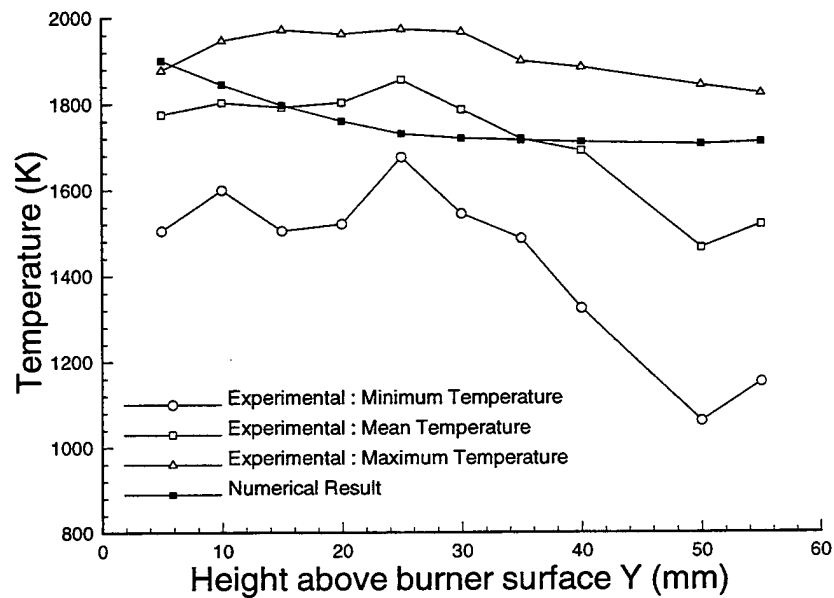
Fig. 18. Comparison of numerically predicted and experimentally measured temperature profiles as a function of distance above the burner surface for the interaction of 3% mass fraction, 50μ water mist droplets with the diffusion flame. The numerical result is the maximum temperature measured at a given height above the burner surface. The experimentally measured maximum, mean and minimum temperatures are the maximum values at a given height.
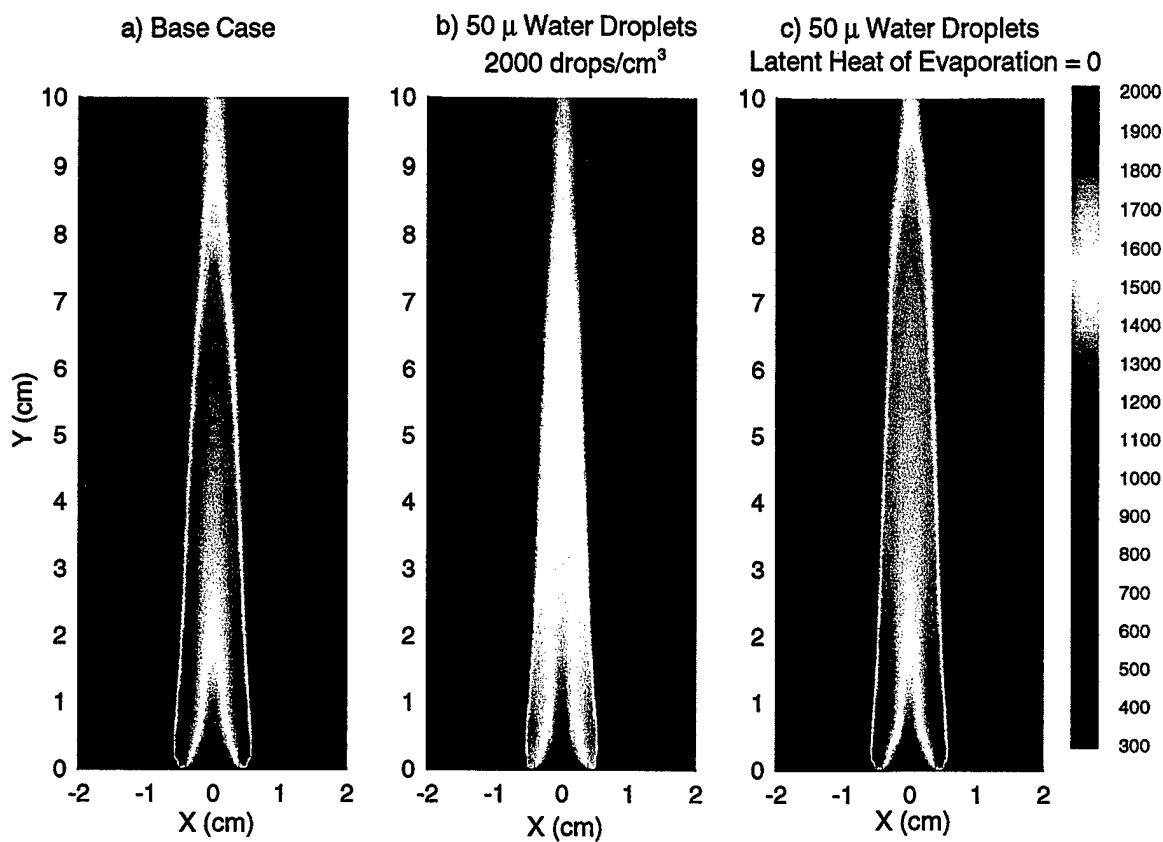
Fig. 19. Temperature contours above a methane-air diffusion flame. a) Base case contours, b) Temperature contours during the injection of 50μ water droplets with a spray injection density of 2000 $drops/cm^3$, c) Same as case b) but with latent heat of evaporation set to zero. These contours illustrate the effect of the various suppression mechanisms.

50μ Water Droplets
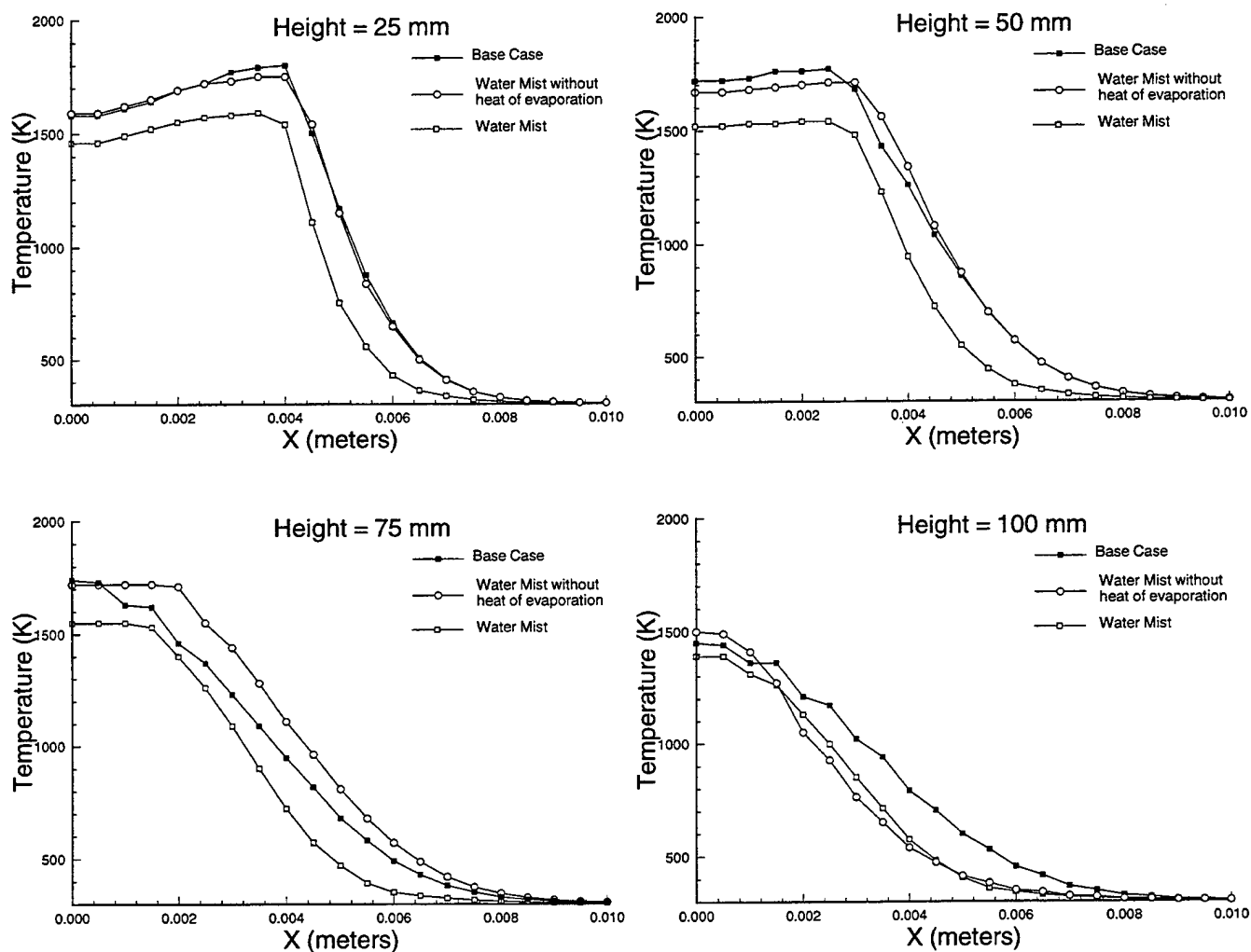
Fig. 20. Temperature profiles at various heights above the burner surface (for the three cases discussed in the previous figure. showing the relative contribution of the various suppression mechanisms such as oxygen dilution and the thermal cooling. Water mist droplets are 50μ diameter.
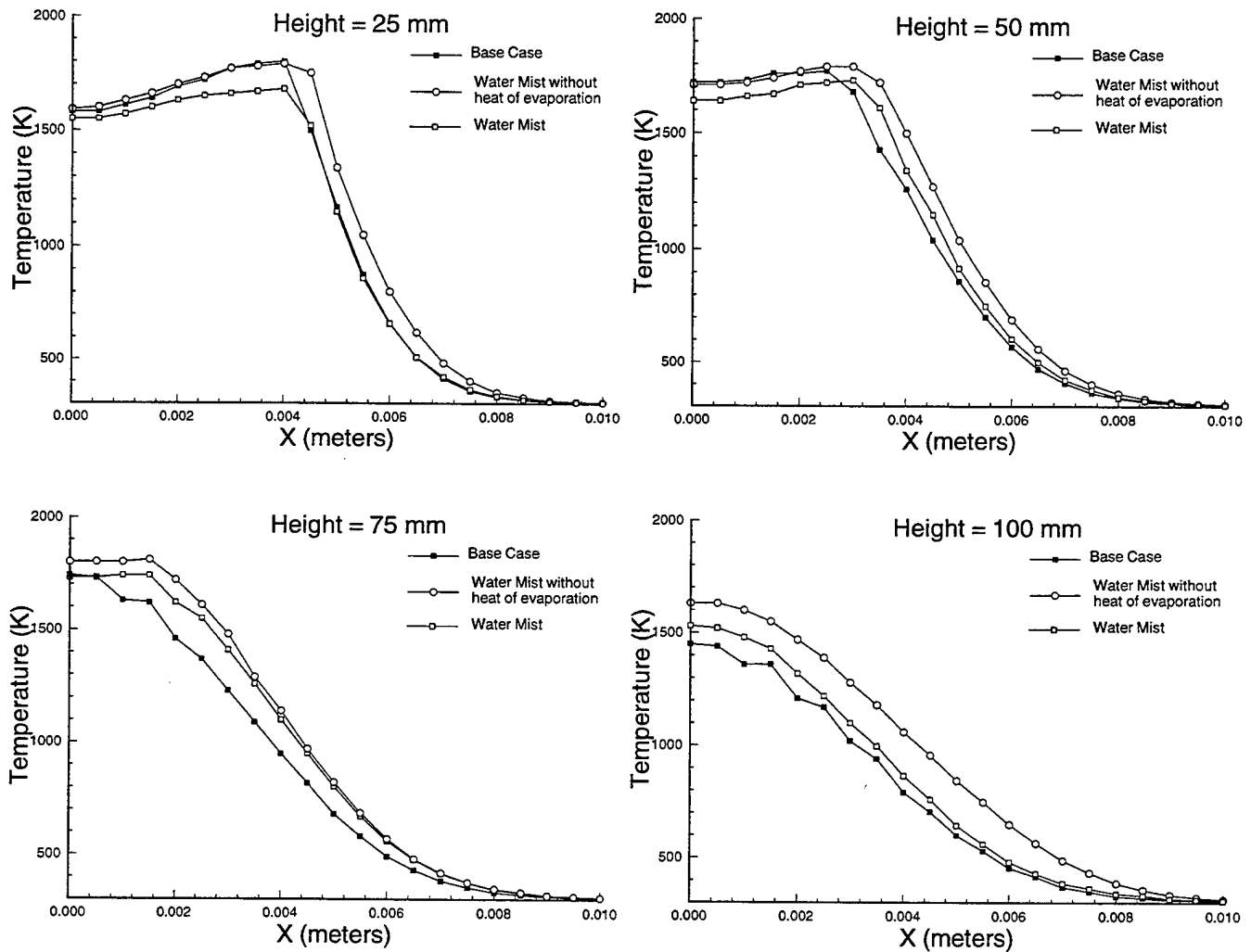
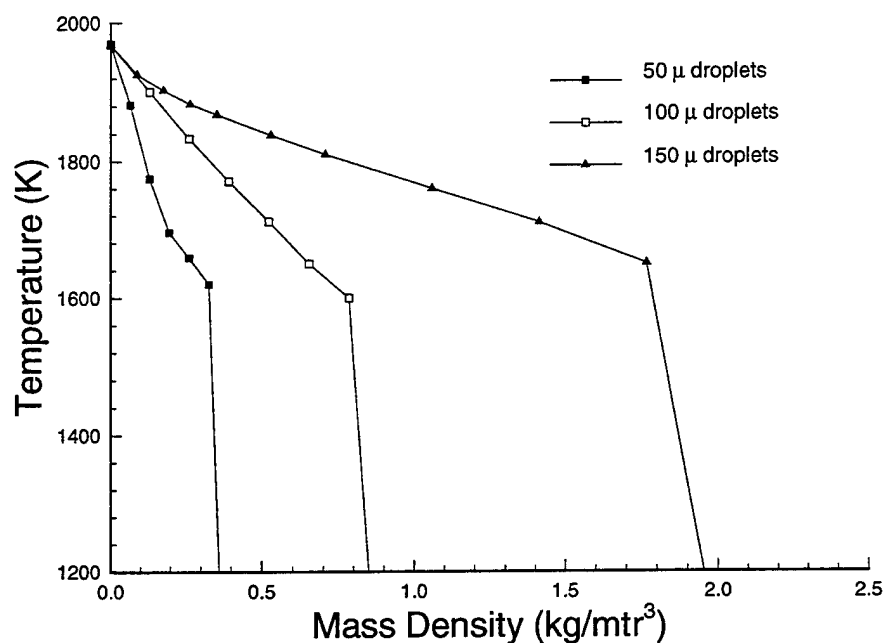Fig. 21. Temperature profiles at various heights above the burner surface (for the three cases discussed in the previous figure. showing the relative contribution of the various suppression mechanisms such as oxygen dilution and the thermal cooling. Water mist droplets are 150μ in diameter.
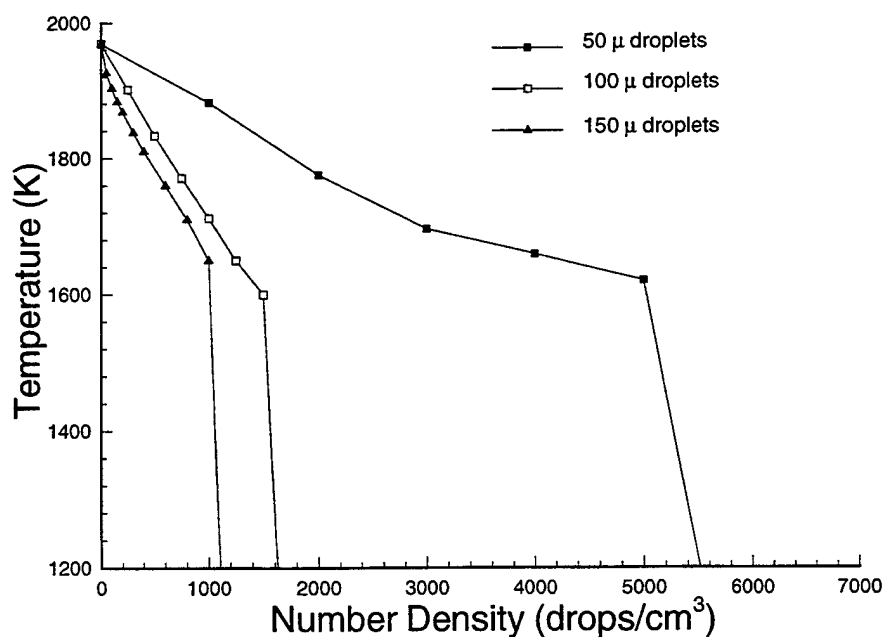
Fig. 22. Suppression/extinction of methane-air diffusion flames during injection of water mist along with the air co-flow. Figure shows the reduction in maximum flame temperature as a function of spray mass density for various droplet diameters.
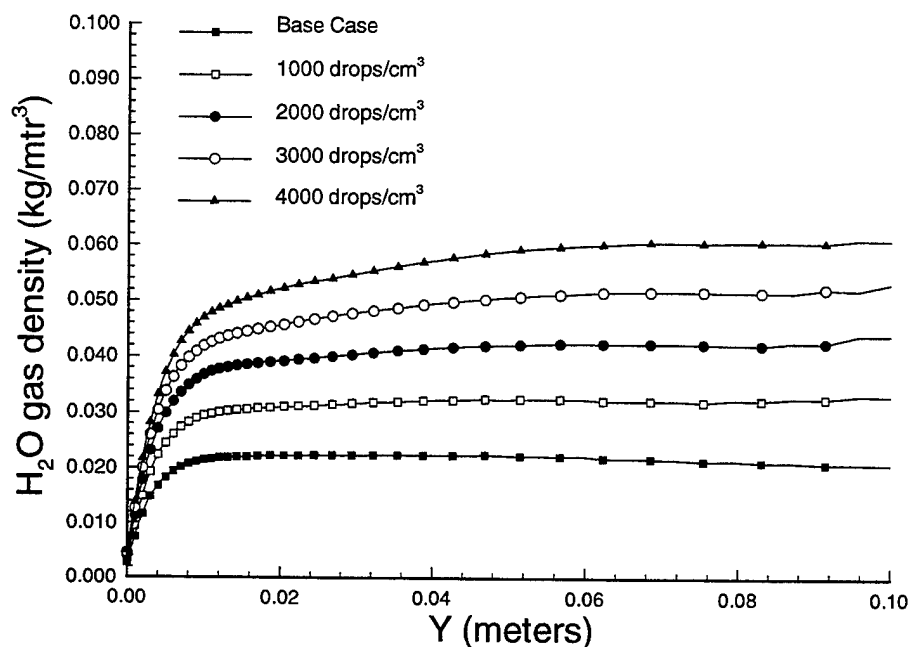

Fig. 23. Suppression/extinction of Methane-Air diffusion flames during injection of water mist along with the air co-flow. Figure shows the reduction in maximum flame temperature as a function of droplet number density for various droplet diameters.

Fig. 24. Center line H_2O gas density profile as a function of distance above the burner surface for various spray injection densities of 50μ water droplets. Also shown is the base case profile indicating the degree of entrainment of water mist into the flame.
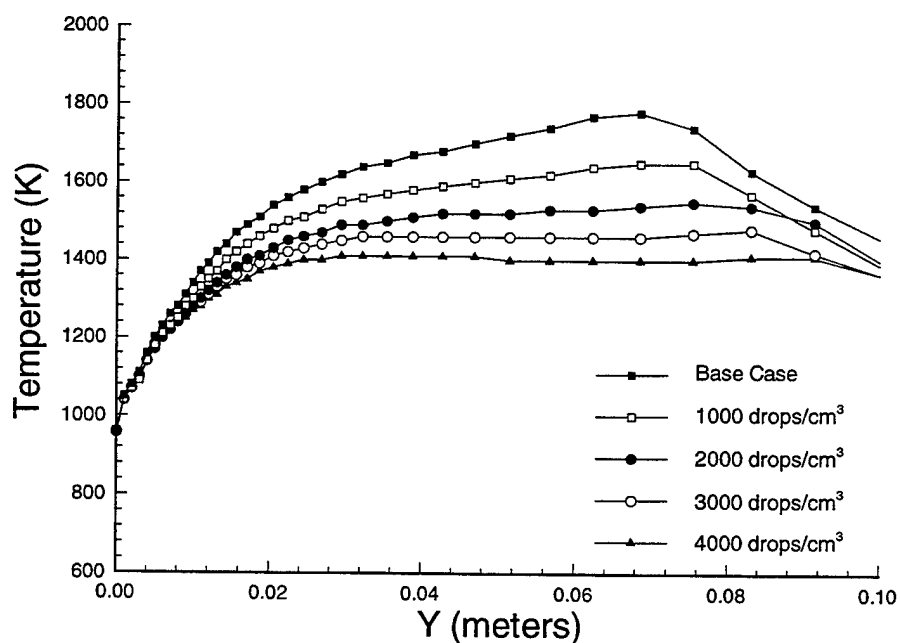

Fig. 25. Center line temperature profile as a function of distance above the burner surface for various spray injection densities of 50μ water droplets. Also shown is the base case profile indicating the suppression in flame temperature due to injection of water mist.
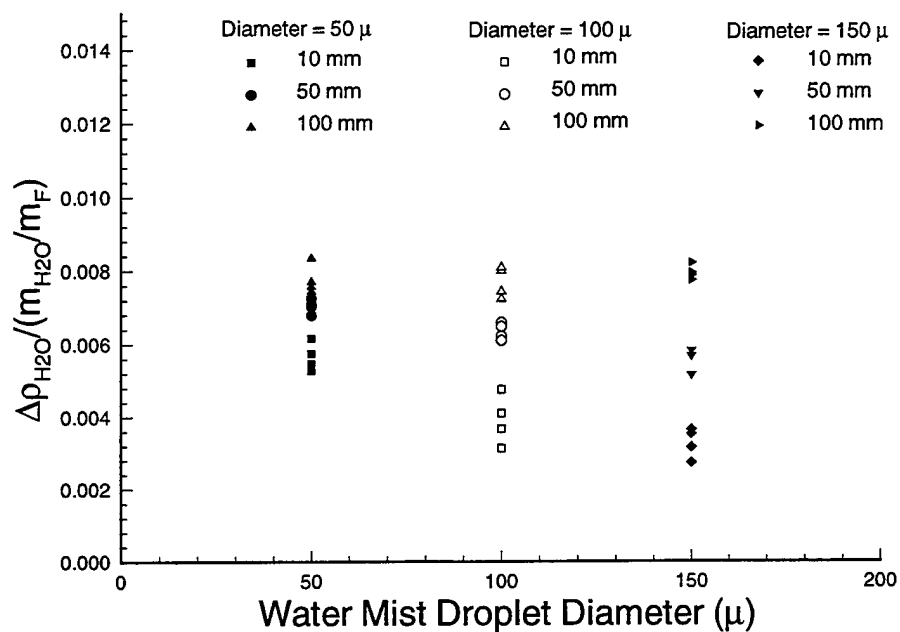
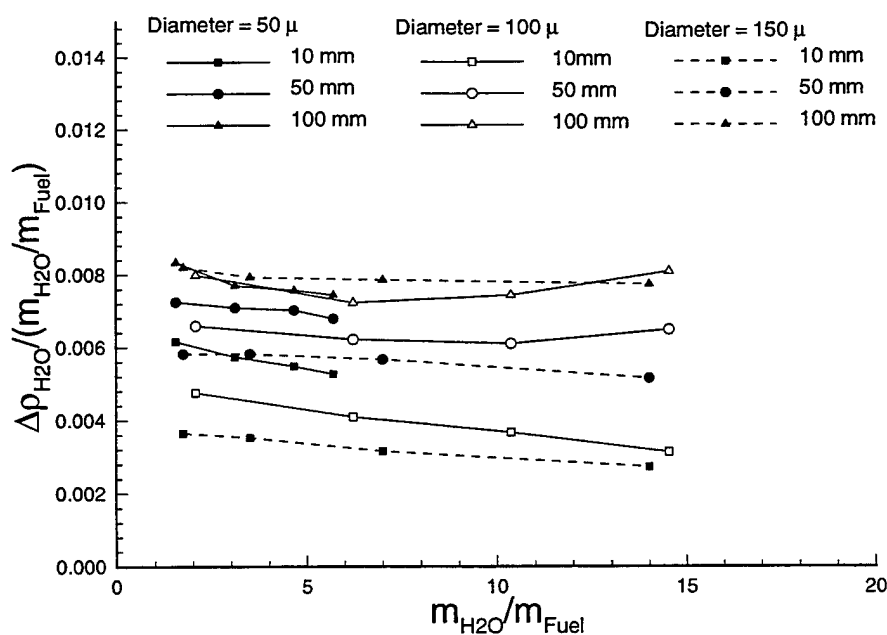Fig. 26. Effect of droplet diameter on water mist entrainment.

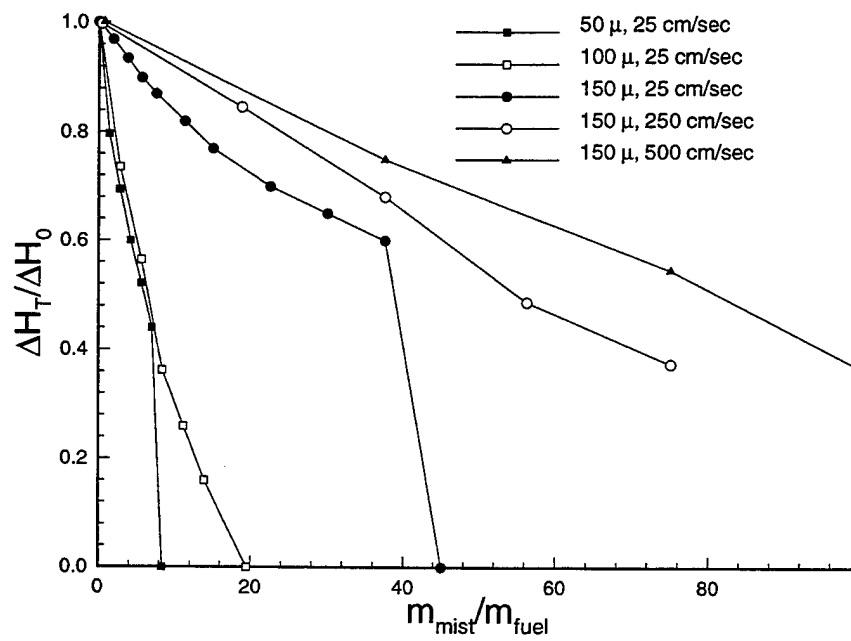Fig. 27. Effect of droplet diameter and injection spray density on water mist entrainment.

Fig. 28. Integrated effect of water mist on diffusion flames. The figure shows the net suppression effect of water mist and its dependence on injection spray density and velocity. The effect of droplet diameter on suppression has also been shown.